J. Mech. Phys. Solids 218 (2027) 106842

Contents lists available at ScienceDirect

Journal of the Mechanics and Physics of Solids

journal homepage: www.elsevier.com/locate/jmps

Peeling and snap-through instability of multilayer 2D blisters with dual interfacial slips

Xiangtian Shen, Zhaohe Dai, Yueguang Wei*

School of Mechanics and Engineering Science, Peking University, Beijing, 100871, China

ARTICLE INFO

Keywords:
J-integral
Configurational mechanics
Multilayer 2D materials
Blister peeling
Snap-through instability
Interfacial fracture

ABSTRACT

The blister peeling process of multilayer two-dimensional (2D) materials is dually regulated by interlayer and substrate slips, rendering the analytical description of the underlying separation mechanism challenging. Within the framework of Eshelby configurational mechanics, this study formulates a generalized J-integral for the interfacial energy release rate that is compatible with shear-mediated large-deflection bending, and applies it to the axisymmetric blister peeling analysis of multilayer 2D structures. By extracting the global configurational driving force, the regulatory mechanisms of multiple interfacial slips on the peeling behavior are revealed, and the blister aspect ratio evolution and load-response relations during the peeling process are quantitatively established. Furthermore, by incorporating parameter dimension-reduction approximations and phase-space analysis, an inversely proportional load–displacement scaling law during the quasi-static peeling stage is derived, and a universal geometric criterion for the onset of snap-through instability under constant-source loading (i.e., fixed gas amount) is formulated. This analytical model not only provides a theoretical basis for accurately extracting the intrinsic multilayer-substrate adhesion energy, but also establishes quantitative criteria for predicting blister peeling responses and guiding instability-resistant designs.

1. Introduction

In recent years, owing to their exceptional mechanical and physical properties, two-dimensional (2D) materials have demonstrated immense potential in the miniaturization frontiers of electronic devices, such as micro/nano-electromechanical systems (MEMS/NEMS) (Liu et al., 2026b; Geng et al., 2026), advanced microprocessors (Guo et al., 2026; Wang et al., 2025), and smart sensors (Vidhi and Yadav, 2026; Thomas et al., 2026). During the large-area integrated manufacturing (Hu et al., 2025) and practical operation of these advanced micro/nano systems, the surface and interfacial mechanical behaviors of 2D materials — particularly the interfacial adhesion and separation mechanisms on substrate surfaces (Brotons-Alcázar et al., 2024; Schätz et al., 2024; Li et al., 2025) — play a crucial role. Due to their extremely low physical thickness and bending stiffness, 2D materials are highly susceptible to out-of-plane deformation (Sanchez et al., 2018; Wang et al., 2019; Liu et al., 2025). This is not only their primary mode of responding to external constraints (Yildirim et al., 2025), but also the core pathway for implementing strain engineering to precisely modulate their physical properties, including phononic (Kim et al., 2025), piezoelectric (Liu et al., 2026a), and optoelectronic (Ai et al., 2025; Zhu et al., 2026) characteristics. Among various out-of-plane morphologies, blisters represent a prototypical closed-confinement geometry that not only provides a natural platform for nanoscale physical and chemical modulation (Sanchez et al., 2021) — such as inducing pseudo-magnetic fields (Dai et al., 2022; Yu et al., 2024), regulating piezoelectric responses (Yao et al.,

* Corresponding author.
E-mail address: weiyg@pku.edu.cn (Y. Wei).

https://doi.org/10.1016/j.jmps.2026.106842
Received 9 June 2026; Received in revised form 9 August 2026; Accepted 5 September 2026
Available online 7 September 2026

2024), and reconstructing electronic band structures (Long et al., 2023) — but also serves as the mainstream mechanical characterization technique for accurately determining the interfacial fracture toughness and intrinsic adhesion energy of 2D thin films (Yue et al., 2012; Wang et al., 2022; Cui et al., 2023). During large-deflection evolution processes such as blister peeling, the mechanical responses of 2D systems are significantly regulated by complex surface and interfacial interactions, including substrate friction and adhesion, as well as interlayer shear. Therefore, elucidating the blister peeling mechanisms under multiple constraints is essential for accurately extracting interfacial adhesion parameters and guiding advanced micro/nano interfacial engineering.

Recent thin-film adhesion theories based on generalized Tabor parameters (Yu et al., 2025; Zeng et al., 2026) indicate that when the macroscopic characteristic scale of a 2D system is significantly larger than the cohesive zone length, the interfacial separation process satisfies strict scale-separation conditions and converges to the JKR limit. Given that the macroscopic blisters in practical multilayer 2D materials typically range from hundreds of nanometers to micrometers in size (Wang et al., 2022; Rao et al., 2023), their peeling evolution evidently fulfills this physical prerequisite. Consequently, in the theoretical modeling of blister peeling, it has become a general consensus to neglect finite process zone effects and adopt a sharp-interface fracture model based on the energy balance condition $G = G_c$ (where G and G_c are the energy release rate and interfacial fracture toughness, respectively). This provides a clear mechanical basis for extracting the interfacial adhesion energy through macroscopic blister morphologies. For single-layer 2D materials idealized as moment-free membranes, Dai et al. (2018) utilized variational methods to investigate the physical limits of both perfectly bonded and absolutely smooth substrates. Together with the extended Hencky series solutions formulated by Ma et al. (2018), these studies established the blister morphological characteristics dominated by stretching energy and interfacial adhesion energy. Their work elucidated the underlying physical mechanism of extracting interfacial properties via the geometric aspect ratio (the ratio of blister height to radius). Subsequently, Sanchez et al. (2018) and Yin et al. (2024) further incorporated finite substrate sliding friction in the supported region and finite deformation effects in the blister region into this energy-balance-driven morphological evolution framework.

Regarding the blister peeling of multilayer 2D materials, traditional theories mostly treat them as large-deflection Föppl–von Kármán (FvK) plates with constant bending stiffness (Wang et al., 2022; Li et al., 2024), aiming to capture the influence of tension-bending coupling on the peeling driving force and subsequent responses during deformation (Rao et al., 2023). Compared to the continuous refinement of single-layer models in terms of mechanical boundaries and numerical methods, existing theoretical descriptions of multilayer blisters still exhibit significant physical limitations. Due to the extremely low interlayer shear stiffness of real multilayer 2D materials, their bending is inevitably accompanied by significant relative interlayer slip. In such systems, the macroscopic bending resistance is primarily generated by interlayer shear mediating stretching gradients, causing their apparent bending stiffness to be substantially lower than the predictions of classical plate theory (Wang et al., 2019; Lee et al., 2022).

In recent years, numerous theoretical studies have emerged exploring the large-deflection slip-mediated bending behavior of multilayer film and plate systems under fixed or sliding-only boundaries (Qin et al., 2020; Liu et al., 2025; Shen and Wei, 2026; Huang et al., 2023). However, these studies are primarily confined to solving the deformation fields within static geometric domains where boundary peeling does not occur. In physical essence, the interfacial evolution of multilayer blisters is a moving boundary problem driven by global energy release. Under the coupling effect of multiple slips (i.e., the coexistence of interlayer slip in the blister region and substrate slip in the supported region), analytically determining the global energy release rate during the migration of the peeling front to elucidate the macroscopic peeling mechanism remains a theoretical void. Specifically, the coupling between large-deflection geometric nonlinearity and multiple interfacial shear-lag effects under moving boundary conditions renders the explicit extraction of the macroscopic peeling driving force mathematically intricate. If this analytical barrier cannot be overcome at the theoretical level, the extraction of intrinsic multilayer-substrate adhesion energy from blister experiments is inherently obscured by apparent stiffness softening effects, thereby compromising the accuracy of interfacial mechanical characterization. Furthermore, the absence of rigorous peeling and instability criteria for such slip-coupled systems limits the reliable design of advanced micro/nano confined structures, impeding the quantitative prediction of complex nonlinear mechanical responses, such as snap-through instability, in engineering applications.

Examining the physical essence of energy drive and configurational evolution, solving such interface peeling problems coupled with multiple slips fundamentally relies on a rigorous theoretical framework of configurational mechanics (Eshelby, 1951; Rice, 1968; Gurtin, 2000). For a multilayer system that simultaneously intertwines in-plane stretching, large-deflection bending, and interlayer shear, to quantify the system energy release rate governing the propagation of the peeling front, this study formally derives a generalized J-integral — compatible with Föppl–von Kármán geometric nonlinearity and Mindlin–Reissner cross-sectional kinematics — based on the generalized Eshelby configurational stress tensor (the detailed derivation is provided in Section S1 of the Supplementary material). On this theoretical basis, the generalized integral is applied to an axisymmetric pressurized blister model of multilayer 2D structures to independently investigate the differential mechanical effects of linear elastic interlayer and substrate slips on interfacial peeling. By analytically extracting the global configurational driving force and establishing a quasi-static peeling criterion, combined with parameter dimension-reduction approximations and phase-space analysis, an inversely proportional load–displacement scaling law during the peeling stage is quantitatively revealed across the full parameter space, and a universal geometric criterion for triggering snap-through instability under constant-source loading is formulated. Furthermore, the evolution laws and instability characteristics predicted by this analytical model are systematically compared with experimental observations in existing literature and molecular dynamics (MD) simulation results from this study, comprehensively validating the rigor of the theory and the accuracy of its predictions.

The remainder of this paper is organized as follows. Section 2 introduces the configurational mechanics framework for the multilayer blister peeling system coupled with multiple slips, deriving the generalized J-integral and the global analytical expression

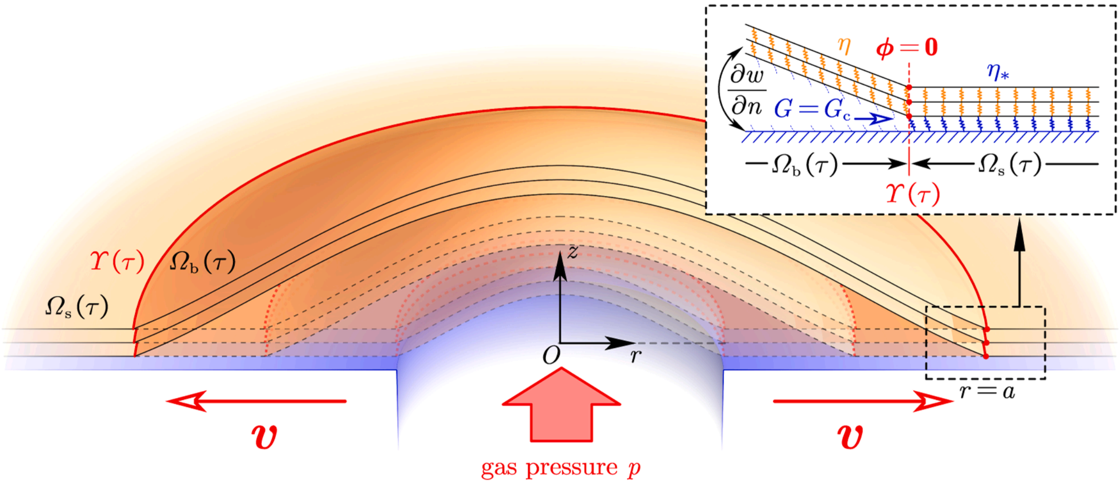

Fig. 1. Schematic of the substrate blister peeling and moving boundary evolution model for multilayer 2D structures. The main panel displays the three-dimensional blister configuration driven by a uniform pressure p, along with the historical traces of the peeling front $\Upsilon(\tau)$ progressively propagating toward the outer supported region ($\Omega_s(\tau)$) with pseudo-time τ. The top-right inset presents an equivalent 2D mechanical magnification of the local interfacial crack tip, illustrating the local peeling configuration driven by the configurational phase velocity $\boldsymbol{v}$. At the peeling front, the kinematic decoupling between the zero cross-sectional rotation ($\boldsymbol{\phi} = \mathbf{0}$) and the non-zero mid-plane slope ($\partial w/\partial n$) is geometrically highlighted. The springs represent the interlayer shear interactions (with stiffness η) within the blister region ($\Omega_b(\tau)$) and the interfacial shear interactions (with stiffness η_*) in the supported region, respectively. The flexural slope $\partial w/\partial n$ at the peeling front and the energy-dominated fracture criterion governed by the interfacial fracture toughness G_c are also indicated.

for the interfacial energy release rate. Section 3 analyzes the geometric evolution, load response, and constant-source snap-through instability mechanism during quasi-static peeling. Finally, Section 4 summarizes the entire paper.

2. Theoretical model

2.1. Mechanics of slip-coupled blister peeling

Consider a multilayer structure composed of N stacked two-dimensional (2D) films with equal interlayer spacing t, where the intrinsic thickness of each layer is neglected and the single-layer tensile stiffness is denoted by E_{2D}. Accordingly, the total tensile stiffness is defined as $E^{\dagger}_{2D} = NE_{2D}$, the total thickness of the multilayer film as $t_{\dagger} = Nt$, and the equivalent bulk Young's modulus as $E = E_{2D}/t$. Driven by a uniform pressure p, this structure undergoes an axisymmetric blister peeling evolution on a rigid substrate. The geometric characteristics and the physical configuration of the interfacial fracture of the system are illustrated in Fig. 1. As the interfacial debonding process proceeds, the core feature of the system manifests as the quasi-static migration of the current debonding radius a, which acts as the evolution boundary (i.e., the peeling front $\Upsilon(\tau)$), thereby spatially dividing the entire multilayer structure into an inner blister region $\Omega_b(\tau)$ and an outer supported region $\Omega_s(\tau)$. It should be particularly noted that, although the present model is established on a quasi-static assumption (i.e., neglecting the inertial effects of material particles), an evolution parameter τ and a phase velocity of the peeling front $\boldsymbol{v} = \frac{da}{d\tau}\boldsymbol{e}_r$ (where e_r is the radial unit vector) are introduced. Here, τ is essentially a pseudo-time parameter characterizing the configurational evolution of the system, and $\boldsymbol{v}$ is not the physical moving velocity of actual material particles, but rather the configurational phase velocity representing the migration of the geometric boundary in the configurational space. It should be explicitly clarified that τ is purely a formal bookkeeping parameter of the configurational description, inherited from the generalized moving-boundary framework (which accommodates arbitrary, non-axisymmetric boundary evolutions) established in the Supplementary Material Section S1. For the specific axisymmetric blister problem solved in the main text, the current debonding radius a naturally serves as the monotone evolution coordinate. Thus, the formal parameter τ can be strictly simplified to $\tau = a$ (yielding $\boldsymbol{v} = \boldsymbol{e}_r$) without losing any physical information, and the extracted energy release rate is inherently independent of this specific reparametrization.

Given that the configurational dimensions of macroscopic blisters in multilayer 2D materials typically range from hundreds of nanometers to micrometers (Rao et al., 2023; Wang et al., 2022) — significantly larger than the atomic-scale cohesive zone length at the peeling front — this work adopts a sharp-interface fracture model based on the small-scale cohesive zone assumption. This implies that the quasi-static peeling propagation process is entirely governed by the macroscopic energy balance condition $G = G_c$, where G_c is the equivalent interfacial fracture toughness integrating the evolution of film-substrate, substrate-gas, and gas-film surface energies. It should be explicitly noted that the present theoretical model does not account for the potential influence of varying fracture mode mixity (i.e., phase angle) on the delamination process. In macroscopic interfacial fracture mechanics, fracture toughness generally depends on the mode mixity. However, for 2D material microblister systems, the aspect ratio (h/a) consistently remains at a very small magnitude (typically $\leq \mathcal{O}(10^{-1})$), constraining the interfacial separation to occur at exceedingly small peel angles.

Consequently, the mode mixity at the peeling front remains nearly constant throughout the quasi-static propagation. Therefore, consistent with theoretical paradigms established for 2D material blisters (Ma et al., 2018; Yin et al., 2024), treating the equivalent interfacial fracture toughness G_c as a constant material property independent of varying fracture modes is a physically reasonable approximation. Moreover, considering that the pure Mode I fracture toughness generally represents the lower bound of interfacial fracture resistance, taking this constant G_c as the Mode I fracture energy effectively provides a conservative criterion for predicting the peeling evolution. Within this framework, the deformation fields and energy release of the entire multilayer system are not only governed by large-deflection geometric nonlinearity, but also globally dependent on multiple interfacial slip behaviors. To establish a rigorous foundation for the generalized configurational stress tensor, the underlying kinematics are formulated within an invariant tensor framework. This representation transcends the previous complex-variable description (Shen and Wei, 2026) to naturally accommodate the geometric nonlinearities inherent in moving boundaries:

First, within the blister region Ω_b ($r \le a$) experiencing out-of-plane large-deflection bulging, the system fully activates in-plane stretching, out-of-plane bending, and interlayer elastic shear slip. The displacement field within this region is assumed to satisfy a homogenized first-order interlayer slip kinematic constraint, whereby the cross-sectional rotation vector $\boldsymbol{\phi} = \phi_x \boldsymbol{i} + \phi_y \boldsymbol{j}$ (where $\boldsymbol{i}$ and $\boldsymbol{j}$ are the basis vectors) is decoupled from the mid-plane slope ∇w (where $\nabla = \frac{\partial}{\partial x}\boldsymbol{i} + \frac{\partial}{\partial y}\boldsymbol{j}$ is the 2D gradient operator). The corresponding interlayer linear elastic shear stiffness is defined as η. The total strain energy areal density $\mathscr{U}$ of the entire field can be orthogonally decomposed, i.e., expressed as a linear superposition of the in-plane stretching energy $\mathscr{U}_m(\boldsymbol{\varepsilon})$ and the combined bending and interlayer shear energy $\mathscr{U}_p(\boldsymbol{K}, \boldsymbol{\gamma})$ induced by the relative cross-sectional motions. Here, the mid-plane strain $\boldsymbol{\varepsilon}$, the resultant cross-sectional tension $\boldsymbol{\Sigma}$, and the stretching strain energy areal density are uniformly expressed as:

$$\begin{cases} \boldsymbol{\varepsilon} = \dfrac{1}{2}(\nabla \otimes \boldsymbol{u} + \boldsymbol{u} \otimes \nabla) + \dfrac{1}{2}\nabla w \otimes \nabla w \\ \boldsymbol{\Sigma} = \dfrac{E_{2D}^{\dagger}}{1-\nu^2}[(1-\nu)\boldsymbol{\varepsilon} + \nu(\mathrm{tr}\boldsymbol{\varepsilon})\boldsymbol{I}] \\ \mathscr{U}_m(\boldsymbol{\varepsilon}) = \dfrac{1}{2}\dfrac{E_{2D}^{\dagger}}{1-\nu^2}[(1-\nu)\boldsymbol{\varepsilon} : \boldsymbol{\varepsilon} + \nu(\mathrm{tr}\boldsymbol{\varepsilon})^2] \end{cases}, \tag{1}$$

where $\boldsymbol{u}$ and w represent the in-plane displacement vector and out-of-plane deflection of the mid-plane, ν denotes Poisson's ratio, $\boldsymbol{I}$ is the second-order identity tensor, and the operators tr, $\otimes$, and $:$ represent the trace, tensor product, and double dot product, respectively. As the orthogonally decoupled out-of-plane deformation components, the bending curvature tensor $\boldsymbol{K}$ and the transverse shear strain vector $\boldsymbol{\gamma}$, the resultant cross-sectional bending moment $\boldsymbol{\mu}$ and the equivalent resultant shear force $\boldsymbol{V}$, as well as the corresponding bending and shear strain energy areal densities, are comprehensively formulated as:

$$\begin{cases} \boldsymbol{K} = \dfrac{1}{2}(\nabla \otimes \boldsymbol{\phi} + \boldsymbol{\phi} \otimes \nabla), \quad \boldsymbol{\gamma} = \nabla w - \boldsymbol{\phi} \\ \boldsymbol{\mu} = D_0[(1-\nu)\boldsymbol{K} + \nu(\mathrm{tr}\boldsymbol{K})\boldsymbol{I}], \quad \boldsymbol{V} = D_{\mathrm{shear}}\boldsymbol{\gamma} \\ \mathscr{U}_p(\boldsymbol{K}, \boldsymbol{\gamma}) = \dfrac{1}{2}D_0[(1-\nu)\boldsymbol{K} : \boldsymbol{K} + \nu(\mathrm{tr}\boldsymbol{K})^2] + \dfrac{1}{2}D_{\mathrm{shear}}|\boldsymbol{\gamma}|^2 \end{cases}, \tag{2}$$

where the equivalent shear stiffness is $D_{\mathrm{shear}} = (N-1)\eta t^2$, and the theoretical upper limit of the cross-sectional bending stiffness is $D_0 = \left(1 - 1/N^2\right)Et_{\dagger}^3/[12(1-\nu^2)]$. Regarding the interlayer coupled mechanical mechanism, the macroscopic bending resistance of the multilayer structure is essentially generated by interlayer shear interactions mediating in-plane stretching gradients. It can be directly observed from the above macroscopic energy expressions that when interlayer slip is completely locked (i.e., $\eta \to \infty$ leading to $D_{\mathrm{shear}} \to \infty$), the transverse shear strain must strictly approach zero ($\boldsymbol{\gamma} \to \boldsymbol{0}$) to ensure a finite total strain energy of the system. Under this condition, the mid-plane rotation $\boldsymbol{\phi}$ converges to the deflection gradient ∇w, and the mid-plane kinematics degenerates to the classical Föppl–von Kármán (FvK) large-deflection plate theory satisfying the Kirchhoff straight-normal assumption.

Second, within the unpeeled supported region Ω_s ($r \ge a$), the multilayer film is subjected to strong out-of-plane displacement constraints from the rigid substrate, exhibiting a purely in-plane linear stretching state (i.e., physical boundary constraints $w = 0, \boldsymbol{\phi} = \boldsymbol{0}$ are introduced). Because the tension in the blister region pulls the material inward, tangential relative elastic slip constraints are activated between the multilayer structure and the substrate, with the interfacial slip stiffness defined as η_* (equivalent to a distributed surface traction $\boldsymbol{f} = -\eta_* \boldsymbol{u}$). In this case, the out-of-plane nonlinear terms and interlayer deformations vanish, and the total energy areal density in this region naturally simplifies to the pure in-plane stretching component $\mathscr{U} = \mathscr{U}_m(\boldsymbol{\varepsilon})$.

The aforementioned domain-wise energy expressions provide a theoretical basis for constructing the configurational driving force at the peeling front in subsequent sections. To quantify the relative strengths of these two slip effects, the interlayer shear-lag characteristic length ℓ and the substrate shear-lag characteristic length ℓ_* are introduced:

$$\ell = \left[\frac{(1-\nu^2)\eta}{Et}\right]^{-\frac{1}{2}}, \quad \ell_* = \left[\frac{(1-\nu^2)\eta_*}{Et}\right]^{-\frac{1}{2}}. \tag{3}$$

In physical essence, these two characteristic lengths directly delineate the intrinsic proportional relationship of the local interlayer and substrate interfacial slip stiffnesses relative to the in-plane tensile stiffness of the single-layer film. Building upon this, and further based on the current debonding radius a, two global dimensionless shear factors, κ and κ_*, are defined:

$$\kappa = a\sqrt{\frac{D_{\mathrm{shear}}}{D_0}} = \frac{2\sqrt{3}}{\sqrt{N(N+1)}}\frac{a}{\ell}, \quad \kappa_* = a\sqrt{\frac{\eta_*}{E_{2D}^{\dagger}/(1-\nu^2)}} = \frac{1}{\sqrt{N}}\frac{a}{\ell_*}. \tag{4}$$

Through the ratios of the configurational characteristic dimension (a) to the shear-lag characteristic lengths (ℓ, ℓ_*), these two dimensionless factors jointly characterize the relative significance of the multiple shear-lag effects within the system.

For the sake of brevity, the full-field solutions of the nonlinear blister derived based on the above kinematic framework are not elaborated here; instead, their specific axisymmetric perturbation solutions are detailed in Section S2 of the Supplementary material.

2.2. Generalized J-integral and energy release rate

After establishing the domain-wise energy framework for the slip-coupled multilayer system, quantifying the energy release mechanism governing interfacial propagation constitutes the theoretical core of the blister peeling model. Specifically, both the substrate interfacial separation and the migration of the interlayer slip front in the multilayer system are, in physical essence, typical moving boundary configurational evolution problems. The migration of these physical boundaries with the evolution parameter τ (at a phase velocity $\boldsymbol{v}$) directly drives the release of the system's total potential energy Π. During the equilibrium propagation process, the negative rate of change of the total potential energy with respect to the evolution parameter ($-\mathrm{d}\Pi/\mathrm{d}\tau$) physically represents the energy release rate in the sense of an evolution rate (i.e., configurational power). By projecting this global rate onto the area swept by the migrating boundary, the conventional local energy release rate defined per unit area (i.e., the local configurational driving force) can be rigorously extracted.

Based on the variational principle of configurational mechanics, a generalized Eshelby configurational stress tensor $\boldsymbol{P}$ compatible with the total strain energy areal density $\mathscr{U}(\boldsymbol{\varepsilon}, \boldsymbol{K}, \boldsymbol{\gamma})$ of the aforementioned slip-coupled multilayer system is introduced:

$$\boldsymbol{P} = (\mathscr{U} - \boldsymbol{f}\cdot\boldsymbol{u} - qw)\boldsymbol{I} - \boldsymbol{\Sigma}\cdot(\boldsymbol{u}\otimes\nabla + \nabla w\otimes\nabla w) - \boldsymbol{\mu}\cdot(\boldsymbol{\phi}\otimes\nabla) - \boldsymbol{V}\otimes\nabla w, \tag{5}$$

where $\boldsymbol{f}$ and q are the distributed in-plane load vector and out-of-plane load scalar within the domain, respectively. Because the peeling and slip fronts topologically manifest as an internal dynamic boundary $\Upsilon(\tau)$ separating different deformation subdomains, there exist discontinuous jumps in deformation modes and external loads across this boundary. Consequently, the rate of change of the system's total potential energy under this specific evolving configuration can be expressed as a linear superposition of two components: a power integral (J-integral) of the jump of the generalized Eshelby configurational stress tensor across the moving boundary $\Upsilon(\tau)$ (i.e., the local configurational driving force) doing work on the phase velocity $\boldsymbol{v}$, and an additional work term induced by the geometric stretching of the boundary curve:

$$\frac{\mathrm{d}\Pi}{\mathrm{d}\tau} = \int_{\Upsilon(\tau)} \boldsymbol{n}\cdot[\![\boldsymbol{P}]\!]\cdot\boldsymbol{v}\mathrm{d}s - \int_{\Upsilon(\tau)} \left(\boldsymbol{T}_\Upsilon\cdot\boldsymbol{u} + V_\Upsilon w + \boldsymbol{M}_\Upsilon\cdot\boldsymbol{\phi}\right)\left(\nabla_\Upsilon\cdot\boldsymbol{v}\right)\mathrm{d}s, \tag{6}$$

where $\boldsymbol{n}$ denotes the unit outward normal vector of the subdomain $\Omega^+(\tau)$ separated by the moving boundary $\Upsilon(\tau)$, and $[\![\cdot]\!] = (\cdot)^+_\Upsilon - (\cdot)^-_\Upsilon$ represents the jump value of the corresponding physical quantity across this boundary. The variables $\boldsymbol{T}_\Upsilon$, V_Υ, and $\boldsymbol{M}_\Upsilon$ represent the distributed in-plane traction, transverse shear force, and bending moment applied along the boundary, respectively. The curve divergence $\nabla_\Upsilon\cdot\boldsymbol{v} = \boldsymbol{e}_s\cdot\frac{\partial \boldsymbol{v}}{\partial s}$ represents the local relative stretching rate of the moving boundary curve ($\boldsymbol{e}_s$ being the tangent vector of the curve). The additional boundary integral term introduced thereby physically reveals the extra potential energy change induced by the distributed line load over the newly created or annihilated arc length due to the geometric stretching of the moving boundary.

Using the Legendre transform, Eq. (6) can be further simplified into a compact integral form containing the jump of the total strain complementary energy areal density:

$$-\frac{\mathrm{d}\Pi}{\mathrm{d}\tau} = \int_{\Upsilon(\tau)} \left[\!\!\left[\mathscr{U}^* + \boldsymbol{f}\cdot\boldsymbol{u} + qw + \frac{1}{2}N_n\left(\frac{\partial w}{\partial n}\right)^2\right]\!\!\right](\boldsymbol{n}\cdot\boldsymbol{v})\mathrm{d}s, \tag{7}$$

where $\mathscr{U}^* = \boldsymbol{\Sigma} : \boldsymbol{\varepsilon} + \boldsymbol{\mu} : \boldsymbol{K} + \boldsymbol{V}\cdot\boldsymbol{\gamma} - \mathscr{U}$ is the total strain complementary energy areal density of the system, and $N_n = \boldsymbol{n}\cdot\boldsymbol{\Sigma}\cdot\boldsymbol{n}$ is the normal membrane tension at the moving boundary. The unique term $\frac{1}{2}N_n\left(\frac{\partial w}{\partial n}\right)^2$ in the above equation is a direct consequence of the Föppl–von Kármán nonlinear geometric characteristics. It reveals that even when the migrating front (e.g., the substrate peeling front) is subjected to an absolute displacement constraint of strictly zero out-of-plane deflection ($w = 0$), the in-plane membrane tension can still contribute to the local potential energy release rate through a local slope discontinuity (forming a geometric kink). The rigorous derivation of the general expressions (Eq. (5) and (6)) and the degenerated form (Eq. (7)) is detailed in Section S1 of the Supplementary material.

Applying Eq. (7) directly to the interfacial fracture analysis of the multilayer blister, the blister region Ω_b and the supported region Ω_s are treated as dynamically evolving subdomains. Since the debonding front strictly satisfies the physical conditions of continuous cross-interface tension and zero out-of-plane deflection and rotation, and considering the linear elastic constitutive relations of the multilayer structure (thus the strain complementary energy $\mathscr{U}^* = \mathscr{U}$), substituting the geometric constraint $(\partial w/\partial n)_{(\mathrm{s})} = 0$ at the peeling front allows the local potential energy release rate per unit peeled area, denoted by A, to be explicitly degenerated from Eq. (7) as:

$$-\left(\frac{\mathrm{d}\Pi}{\mathrm{d}A}\right)_\Upsilon = \left[\!\!\left[\mathscr{U} + \boldsymbol{f}\cdot\boldsymbol{u} + qw + \frac{1}{2}N_n\left(\frac{\partial w}{\partial n}\right)^2\right]\!\!\right] = \mathscr{U}^{(\mathrm{b})} + \frac{1}{2}N_n^{(\mathrm{b})}\left(\frac{\partial w}{\partial n}\right)^2_{(\mathrm{b})} - \mathscr{U}^{(\mathrm{s})} + \frac{1}{2}\eta_* u_\mathrm{s}^2. \tag{8}$$

where the superscripts/subscripts (b) and (s) denote the one-sided limiting values of the corresponding physical quantities as they approach the interface curve Υ from the blister region and the supported region, respectively. It is necessary to clarify that the external work term $-\boldsymbol{f}\cdot\boldsymbol{u}$ in the aforementioned generalized J-integral was derived based on a constant dead load (see Section S1 of the Supplementary material). However, within the supported region of the multilayer blister, the in-plane constraint from the substrate is actually an elastic slip resistance that evolves linearly with displacement ($\boldsymbol{f} = -\eta_* \boldsymbol{u}$). Therefore, the work contribution of this distributed force must be integrated along the displacement path, which physically transforms into the elastic strain energy areal density $\frac{1}{2}\eta_* u_s^2$ stored at the substrate interface.

Furthermore, extracting the limiting values of the full-field perturbation solutions at the boundary edge $\rho = 1$ and substituting them into the local potential energy release rate in Eq. (8), the resulting expression is expanded asymptotically with respect to the small parameter $W_0 = h/a$ (where $h = w(0)$ denotes the out-of-plane central deflection of the blister measured from the undeformed flat reference configuration). After truncating the higher-order infinitesimal terms of $\mathcal{O}(W_0^6)$ and above, the local potential energy release rate can be simplified into a linear superposition of a bending-dominated term and a membrane-tension-dominated term:

$$-\left(\frac{\mathrm{d}\Pi}{\mathrm{d}A}\right)_Y = \frac{32\kappa^4}{(\kappa^2+16)^2} D_0 \frac{h^2}{a^4} + Q_Y(\kappa,\kappa_*,\nu) E_{2\mathrm{D}}^{\dagger} \frac{h^4}{a^4}. \tag{9}$$

Although Eq. (9) provides the energy release contribution at the boundary, it should be pointed out that because the finite-order perturbation solutions within the blister region cannot exactly satisfy the nonlinear differential governing equations, this perturbation truncation error will induce a spurious "energy residual" in the potential energy variation. To ensure the rigor of the global energy release rate theory, in addition to the local boundary term in Eq. (9), the total potential energy release rate must also incorporate a compensation for the integral residual term of the governing equations within the domain:

$$\begin{aligned}(\delta\Pi)_\Omega =& -\frac{\pi D_0}{a}\int_0^1 \left[\kappa^2\left(2\frac{\mathrm{d}W}{\mathrm{d}\rho} - \frac{\Phi}{\rho}\right) + 4\frac{\mathrm{d}^2\Phi}{\mathrm{d}\rho^2}\right]\delta(a\Phi)\mathrm{d}\rho \\ & -\frac{\pi D_0}{a}\int_0^1 \left[4\frac{\mathrm{d}}{\mathrm{d}\rho}\left(\rho S\frac{\mathrm{d}W}{\mathrm{d}\rho}\right) + 2\kappa^2\frac{\mathrm{d}}{\mathrm{d}\rho}\left(2\rho\frac{\mathrm{d}W}{\mathrm{d}\rho} - \Phi\right) + 2P\right]\delta(aW)\mathrm{d}\rho \\ =& -2\pi Q_\Omega(\kappa,\kappa_*,\nu)E_{2\mathrm{D}}^{\dagger}\frac{h^4}{a^3}\delta a.\end{aligned} \tag{10}$$

where the specific definitions of the dimensionless physical quantities (e.g., ρ, W, Φ, S, P) within the integral are detailed in Section S2 of the Supplementary material. It follows that the energy release rate correction term equivalently generated by the non-equilibrium residual within the domain is $-(\mathrm{d}\Pi/\mathrm{d}A)_\Omega = Q_\Omega E_{2\mathrm{D}}^{\dagger}(h/a)^4$.

Consequently, superimposing the local boundary evolution term and the domain residual compensation term yields the analytical expression for the global potential energy release rate of the multilayer 2D structure when both interlayer and substrate slips occur simultaneously:

$$G = -\left[\left(\frac{\mathrm{d}\Pi}{\mathrm{d}A}\right)_Y + \left(\frac{\mathrm{d}\Pi}{\mathrm{d}A}\right)_\Omega\right] = \frac{32\kappa^4}{(\kappa^2+16)^2} D_0 \frac{h^2}{a^4} + Q(\kappa,\kappa_*,\nu) E_{2\mathrm{D}}^{\dagger} \frac{h^4}{a^4}, \tag{11}$$

where the dimensionless stretching release rate coefficient function contributed by large-deflection bending (briefly referred to as the stretching release rate coefficient) is defined as $Q = Q_Y + Q_\Omega$. Given that Q_Y, Q_Ω, and their superposition Q are mathematically highly cumbersome, their complete exact analytical expressions are provided in Section S3 of the Supplementary material. Since their complex analytical forms are inconvenient for direct engineering application, a high-precision approximation for $Q(\kappa,\kappa_*,\nu)$ is proposed in the subsequent Section 3.2, demonstrating its critical role in predicting the peeling response and instability behavior of multilayer 2D structures.

3. Results and discussion

3.1. Geometric evolution of blister peeling

Let a denote the current blister radius during the deformation and peeling process, and define a_c as the critical initiation radius governed by the interfacial energy criterion. During the constant-radius pressurization stage prior to initiation, the boundary Y remains stationary ($a = a_\mathrm{c}$). Once the quasi-static peeling propagation stage is reached ($a > a_\mathrm{c}$), the previously defined central aspect ratio (h/a) is completely governed by the interfacial energy balance. Given the substrate interfacial fracture toughness G_c, according to the energy release rate criterion, the energy governing equation for critical initiation and quasi-static peeling is:

$$G = \frac{32\kappa^4}{(\kappa^2+16)^2} D_0 \frac{h^2}{a^4} + Q(\kappa,\kappa_*,\nu) E_{2\mathrm{D}}^{\dagger} \frac{h^4}{a^4} = G_\mathrm{c}. \tag{12}$$

Denoting this energy-criterion-dominated peeling aspect ratio specifically as W_Y, its evolution law with respect to the debonding radius can be explicitly solved from Eq. (12):

$$W_Y(a) = \left(\frac{\sqrt{1+\beta^2}-1}{\beta}\right)^{\frac{1}{2}} \left[\frac{\mathcal{G}_\mathrm{c}}{Q(\kappa,\kappa_*,\nu)}\right]^{\frac{1}{4}}, \tag{13}$$

where the dimensionless parameters are defined as:

$$\beta = \frac{a^2\sqrt{G_\mathrm{c}E_{2\mathrm{D}}^{\dagger}Q}}{16D_0}\left(\frac{\kappa^2+16}{\kappa^2}\right)^2, \quad \mathcal{G}_\mathrm{c} = \frac{G_\mathrm{c}}{E_{2\mathrm{D}}^{\dagger}}. \tag{14}$$

The shear factors κ and κ_* as functions of a have been given in Eq. (4). It is evident that the aspect ratio equation (Eq. (13)) only involves the intrinsic structural and material parameters of the system, independent of the external loading path. When $a = a_c$, $W_Y(a_c) = W_c$ represents the critical peeling aspect ratio of the blister.

According to Eq. (13), multilayer blisters exhibit a geometric evolution law during the peeling process that is distinctly different from that of single-layer moment-free membranes. Isolating the large-deflection geometric nonlinear effect, two limiting slip states can be examined. When the interlayer is perfectly bonded ($\ell = 0$, leading to a constant structural bending stiffness D_0), the system exhibits a classical large-deflection plate response. In the initial stage with a small a, Eq. (12) is dominated by the bending term, yielding $W_Y \approx \sqrt{G_c/(32D_0)}a$, meaning the aspect ratio is linearly proportional to the peeling radius. As the radius continues to increase, the large-deflection geometric effect gradually increases the contribution of the membrane stretching term, flattening the slope of the curve. Conversely, for the pure membrane limit with completely decoupled interlayers ($\ell = \infty$), the intrinsic bending stiffness of the system completely vanishes (since $\kappa = 0$). The bending-dominated term in Eq. (12) no longer exists, and the deformation of the system is entirely governed by the membrane tension:

$$W_Y = \left[\frac{\mathcal{G}_c}{Q(0, \kappa_*, \nu)}\right]^{\frac{1}{4}}. \tag{15}$$

At this point, the strong dependence of the aspect ratio on the radius a (a characteristic of plate bending) is eliminated, and its evolution is only weakly regulated by the substrate shear factor $\kappa_* \propto a/\ell_*$.

However, for real multilayer systems with a finite slip length ($\ell \neq 0, \infty$), the extension of the peeling radius a not only drives the aforementioned "large-deflection geometric evolution" but also synchronously alters the "structural coupled stiffness" of the system, thereby triggering a dual-dimensional mechanism competition. To further reveal the parametric influence on Eq. (13) under this competition, its asymptotic stationary behaviors at extremely small and extremely large blister dimensions are investigated below. Analyzing the essence of this behavior involves exploring the relative proportional relationship between the macroscopic geometric characteristic dimension a and the intrinsic shear-lag characteristic lengths ℓ and ℓ_*. To this end, the asymptotic values of the stretching release rate coefficient $Q(\kappa, \kappa_*, \nu)$ in various extreme cases are first given (it can be mathematically proven that the limits of Q as its first two independent variables approach 0 and ∞, respectively, are interchangeable in order):

$$\begin{aligned} Q(0,0,\nu) &= \frac{11}{12}, \quad & Q(0,\infty,\nu) &= \frac{37-7\nu}{24(1-\nu)}, \\ Q(\infty,0,\nu) &= \frac{694}{945}, \quad & Q(\infty,\infty,\nu) &= \frac{5879-2449\nu}{5670(1-\nu)}. \end{aligned} \tag{16}$$

Although the energy criterion based on linear elastic fracture mechanics requires $a > a_c$, exploring the mathematical limit $W_Y(0) = \lim_{a\to 0} W_Y(a)$ helps reveal the mechanical degradation mechanism of the multilayer system at extremely small geometric dimensions. Since the interlayer shear factor $\kappa \propto a/\ell$, an extremely small geometric dimension inevitably leads to $a \ll \ell$. This implies that the slip path is too short for the interlayer shear force to be effectively transferred. The multilayer film undergoes structural interlayer decoupling, and its macroscopic bending stiffness approaches zero, thereby exhibiting flexible characteristics akin to a combination of independent films (i.e., $\kappa \to 0$, $\beta \to \infty$). Substituting Eq. (16) into Eq. (13) indicates that the envelope interval of the initial aspect ratio is bounded by:

$$\left[\frac{24(1-\nu)}{37-7\nu}\mathcal{G}_c\right]^{\frac{1}{4}} \le W_Y(0) \le \left(\frac{12}{11}\mathcal{G}_c\right)^{\frac{1}{4}}. \tag{17}$$

The lower bound of the above interval is strictly attained only when the substrate is perfectly bonded ($\ell_* = 0$), whereas the upper bound widely holds as long as there is any arbitrary substrate slippage (i.e., $\ell_* > 0$). Physically, this signifies that at extremely small dimensions, any finite substrate friction cannot accumulate sufficient resistance, and the system will exhibit a flexible-membrane degradation behavior similar to that of a perfectly smooth substrate. Similarly, only when the interlayer is also perfectly bonded ($\ell = 0$ leading to $\kappa = \infty$) will the system maintain a massive intrinsic bending stiffness at extremely small dimensions, thereby yielding the singular pure-plate limit of $W_Y(0) = 0$.

On the other hand, as the blister extends into the large-dimension regime, the final equilibrium propagation envelope is denoted as $W_Y(\infty) = \lim_{a\to\infty} W_Y(a)$. As long as there is non-zero frictional resistance between the layers ($\ell \neq \infty$), a sufficiently long geometric extension will ultimately result in $a \gg \ell$. At this point, the extended slip path allows the interlayer shear forces to be fully transferred and accumulated, triggering a full shear coupling effect. This effect significantly enhances the apparent bending stiffness of the system, such that the multilayer structure no longer behaves as an assembly of decoupled flexible membranes, but rather its mechanical behavior converges toward that of an equivalent monolithic plate (i.e., $\kappa \to \infty$). Through algebraic derivation, the final quasi-static peeling aspect ratio of the system asymptotically approaches the following interval:

$$\left[\frac{5670(1-\nu)}{5879-2449\nu}\mathcal{G}_c\right]^{\frac{1}{4}} \le W_Y(\infty) \le \left(\frac{945}{694}\mathcal{G}_c\right)^{\frac{1}{4}}. \tag{18}$$

To verify the predictive and explanatory capabilities of the proposed theoretical model for the actual peeling morphologies of multilayer 2D materials, the experimental results from Wang et al. (2022) regarding spontaneous blisters of multilayer graphene driven by interfacial water molecules on an hBN surface are introduced for comparison. In Fig. 2, the evolution of the aspect ratio W_Y with the radius a for layer numbers $N \in \{4, 12, 25, 39, 55\}$ is plotted using Eq. (13) (the interfacial fracture toughness is taken as $G_c = 80\,\mathrm{mJ/m^2}$, which falls within the range reported in the literature). The four subfigures display the theoretical comparison results when the interlayer shear-lag characteristic length ℓ is set to 0, 2 nm, 5 nm, and ∞, respectively. For a given number of layers, the theoretical curves form a colored envelope band between an absolutely smooth substrate ($\ell_* \equiv \infty$, upper bound solid line) and a perfectly bonded substrate ($\ell_* \equiv 0$, lower bound dashed line).

From the comparison results, due to the limited distribution range of the experimental data, it is not possible to inversely fit an exact interlayer characteristic length ℓ using a unique set of theoretical curves (as shown in Fig. 2(a) to 2(d), the theoretical envelope bands can cover the distribution range of the experimental data across the entire interval of ℓ from 0 to ∞). Nevertheless, this set of comparisons still substantiates the validity and macroscopic physical predictability of the present theory to a certain extent. First, within the dimension of a single layer number, the theoretical curves accurately capture the nonlinear growth trend of the aspect ratio evolving with the debonding dimension. Second, across the dimension of different layer numbers, the theoretical envelope bands successfully reproduce the vertical stepwise distribution among the five experimental groups, fully reflecting the model's rational characterization of the thickness effect in multilayer structures. Finally, for any given theoretical band of a specific layer number, the experimental data points generally exhibit the most ideal agreement with the upper bound of the band (i.e., the solid line representing the absolutely smooth substrate state). This geometric manifestation at the macroscopic mechanical level is highly consistent with the superlubricity characteristic of the graphene/hBN interface widely reported in the literature.

To further verify the broad applicability and analytical robustness of the interfacial peeling energy criterion proposed in this paper, it is necessary to degenerate the slip-coupled multilayer system to the pure membrane limit with completely decoupled interlayers ($\ell = \infty$), and systematically compare it with the classic theoretical results for moment-free membrane blister peeling. The motivation for selecting this limit as a validation benchmark is twofold: First, the moment-free membrane model is the most prevalent physical assumption in the blister mechanics of single-layer 2D materials; the degeneration analysis can intuitively demonstrate the full compatibility of the established configurational energy framework with existing classical theories. Second, the perturbation solution relied upon to extract the global energy release rate is, in mathematical essence, expanded based on a purely bending linear solution (see Section S2 of the Supplementary material). Therefore, when the macroscopic equivalent bending stiffness of the multilayer system completely vanishes and the large-deflection geometric nonlinearity becomes absolutely dominant (i.e., the pure membrane limit), it poses the most severe test for the aforementioned perturbation solution. If the total potential energy release rate derived based on this perturbation solution can still accurately degenerate and match the existing classical pure membrane solutions under this extreme mechanical state, it will fully substantiate the universality and theoretical rigor of the present analytical criterion.

At $\ell = \infty$ (i.e., $\kappa = 0$), the analytical expression for the stretching release rate coefficient Q significantly simplifies to:

$$Q(0, \kappa_*, \nu) = \frac{17 - 5\nu}{12(1 - \nu)} + \frac{1 + \nu}{1 - \nu}\frac{K_1(\kappa_*)[\kappa_* K_1(\kappa_*) - 8K_2(\kappa_*)]}{8\kappa_* K_2^2(\kappa_*)}. \tag{19}$$

Previous studies on moment-free membrane blisters often relied on complex Hencky series or numerical methods, and were typically confined to extreme boundary assumptions of a perfectly bonded or completely smooth substrate (corresponding to $\kappa_* \to \infty$ and $\kappa_* = 0$ in the present theory, respectively). In Fig. 3, a comprehensive comparison between the theoretical degenerated solutions based on Eq. (19) and previous classic results is presented. Herein, Fig. 3(a) presents the variation of the stretching release rate coefficient Q with the Poisson's ratio ν, while Fig. 3(b) further illustrates the evolutionary relationship of the peeling aspect ratio W_Y with the dimensionless interfacial fracture toughness $\mathcal{G}_c$ at a specific Poisson's ratio ($\nu = 0.174$). The discrete scattered points in the figure summarize the results obtained by previous researchers based on different solution methods under the two extreme substrate slip assumptions. As can be seen from the figure, the upper and lower bound theoretical curves degenerated from the present study (corresponding to $Q(0, 0, \nu) = 11/12$ and $Q(0, \infty, \nu) = (37 - 7\nu)/[24(1 - \nu)]$, respectively) fit flawlessly among the two categories of results obtained by various previous methods, which fully confirms the reliability of the present results in the purely nonlinear regime. It is worth noting that for the pure membrane limit with a perfectly bonded substrate ($\kappa = 0, \kappa_* = \infty$), variational methods utilizing parametric displacement shape functions that constrain the boundary circumferential strain to zero (Yue et al., 2012) can induce an artificial energy divergence due to membrane stretching mode locking as $\nu \to -1$, although they provide concise and accurate approximations for the conventional Poisson's ratio range of engineering materials.

In addition, Fig. 3 also plots three transitional curves of the present theory when the substrate possesses an arbitrary finite shear-lag characteristic (i.e., κ_* ranges between 0 and ∞). These transitional results demonstrate that the derived analytical expression (Eq. (19)) provides a continuous quantitative description of the mechanical transition from perfect bonding to absolute smoothness, extending the analytical framework to accommodate linear elastic substrate slippage.

To more comprehensively and systematically validate the theoretical results regarding multilayer blister peeling, molecular dynamics (MD) simulations are further conducted in this study (specific modeling methods, calibration of interaction potential parameters, and other details are provided in Section S5 of the Supplementary material). Fig. 4 presents a comprehensive comparison between the theoretical predictions of the aspect ratio in this section and the MD simulation results, illustrating the variation of the critical aspect ratio with the dimensionless interfacial toughness $\mathcal{G}_c$. The blue, green, and red theoretical envelope bands in the figure correspond to the interlayer shear-lag characteristic lengths $\ell = 0, 1.0\,\mathrm{nm}$, and $5.0\,\mathrm{nm}$, respectively. It is noteworthy that, because the horizontal axis $\mathcal{G}_c = G_c/E^{\dagger}_{2D}$ is nondimensionalized by the total in-plane tensile stiffness of the multilayer system, when the interlayer shear effect is weak (e.g., the red band for $\ell = 5.0\,\mathrm{nm}$), the envelope position of the theoretical curves is highly similar to that of a single-layer moment-free membrane. As the interlayer shear stiffness increases (ℓ decreases), the theoretical bands gradually narrow while their overall positions shift downward, ultimately approaching the large-deflection plate limit of perfect interlayer bonding (the narrow blue band). The scattered points plotted with hollow symbols represent the simulation results for different substrate characteristic lengths (hollow down-triangles, squares, and up-triangles sequentially correspond to $\ell_* = 1.0\,\mathrm{nm}, 2.5\,\mathrm{nm}, 5.0\,\mathrm{nm}$). Constrained by the

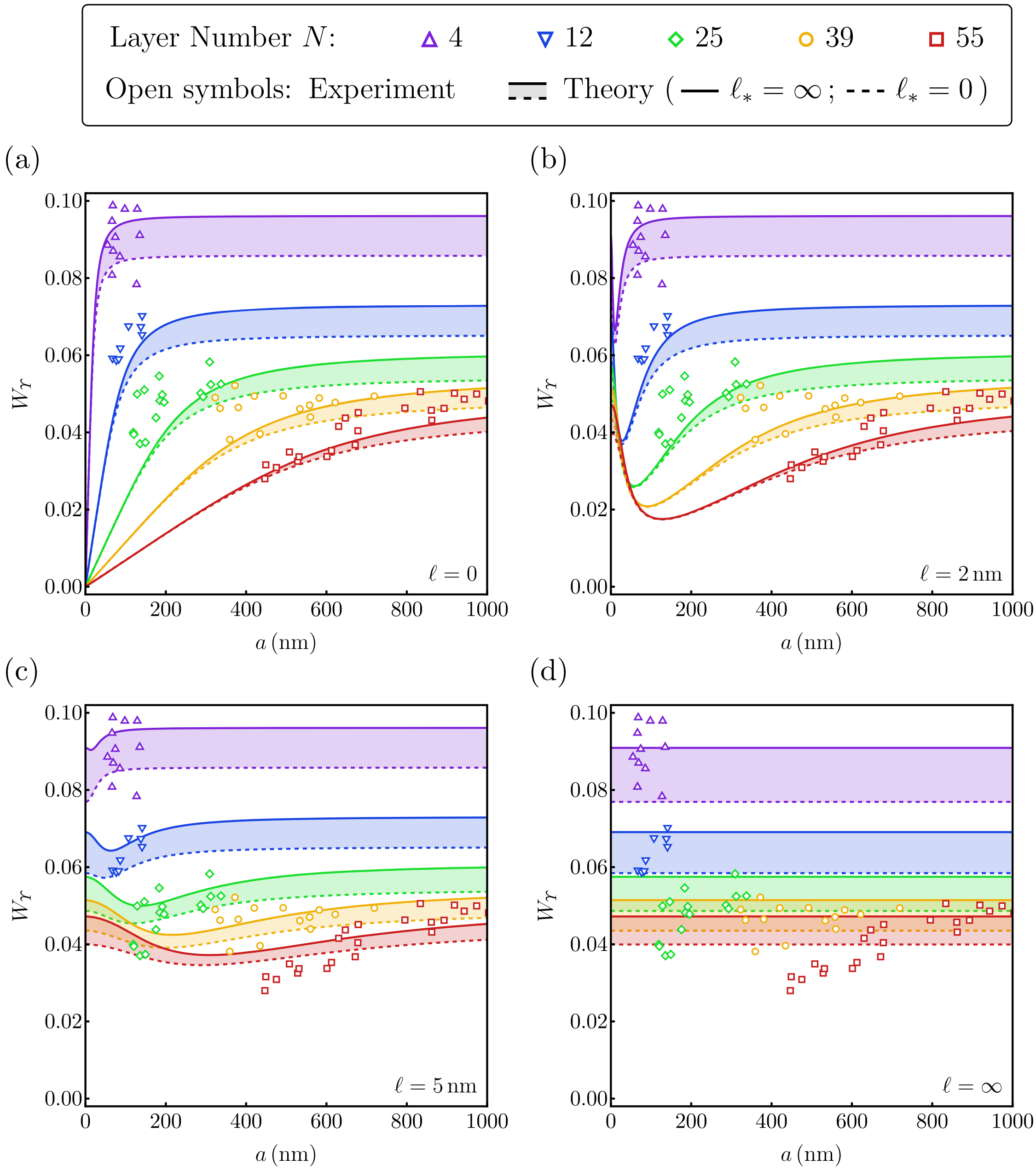

Fig. 2. Comparison between the theoretical curves of blister aspect ratio evolution and the experimental data from Wang et al. (2022). The scattered points represent measured values of multilayer graphene/hBN blisters with different numbers of layers N. For a specific layer number, the colored shaded area denotes its theoretical envelope band, with the upper bound solid line and the lower bound dashed line corresponding to the absolutely smooth ($\ell_* = \infty$) and perfectly bonded ($\ell_* = 0$) substrate limits, respectively. Subfigures (a)–(d) sequentially display the morphologies of the envelope bands assuming different interlayer characteristic lengths ℓ. The experimental data generally agree well with the upper bounds of the envelope bands, corroborating the physical superlubricity of the substrate interface.

numerical stability of the time integration in MD simulations with respect to extremely high interlayer angular spring stiffnesses, the absolute interlayer bonding limit ($\ell = 0$) is difficult to reproduce directly through simulation; thus, the blue band is presented solely as a theoretical lower bound. Meanwhile, given that the theoretical envelope of the green band ($\ell = 1.0\,\mathrm{nm}$) is extremely narrow, only the most representative substrate slip parameters are extracted for plotting the scattered points, ensuring both the completeness of validation and the clarity of the figure. Nevertheless, the existing simulated scattered points essentially fall within their corresponding theoretical bands and intuitively reflect the theoretical expectation that a greater substrate shear stiffness (i.e., a smaller ℓ_*) results in a lower curve position.

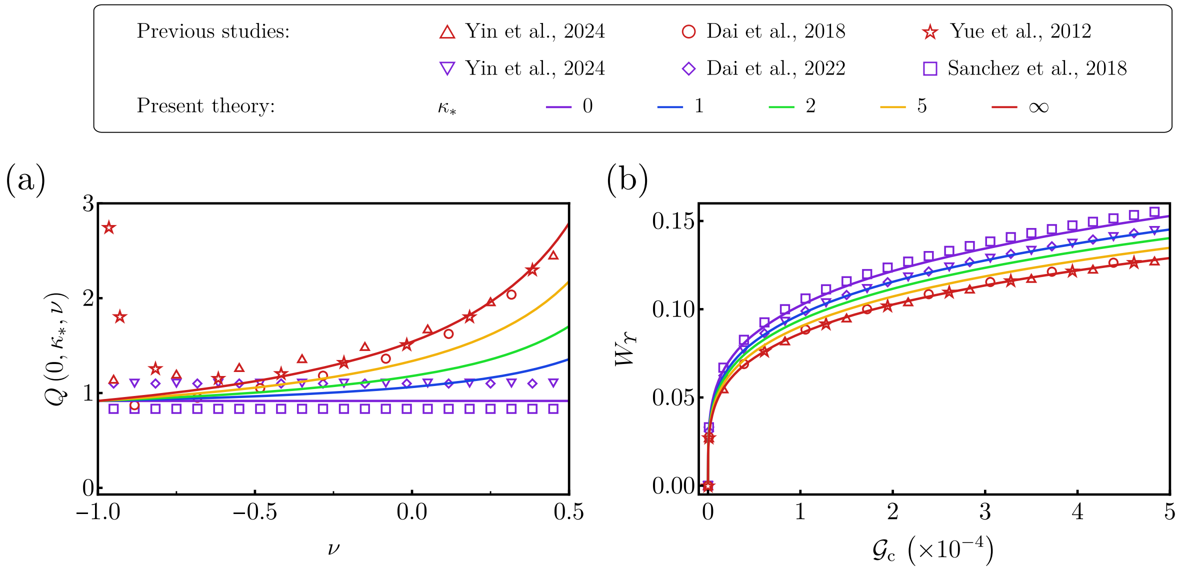

Fig. 3. Systematic comparative validation between the unified theory of this paper and previous research results under the moment-free membrane limit ($\ell = \infty$). The discrete scattered points summarize previous results under the two extreme interfacial slip assumptions of an absolutely smooth (corresponding to the upper bound) and a perfectly bonded (corresponding to the lower bound) substrate based on various solution methods. The cluster of colored solid lines represents the predictive curves of the degenerated analytical solution (Eq. (19)) from the present theory. Subfigure (a) presents the variation of the stretching release rate coefficient Q with respect to the Poisson's ratio ν; Subfigure (b) shows the evolutionary relationship of the critical peeling aspect ratio W_Υ with the dimensionless interfacial fracture toughness $\mathcal{G}_c$ at $\nu = 0.174$. Through the adjustment of κ_*, the analytical theory bridges the two extreme interfacial slip states.

Figs. 4(b) to 4(d) further track the complete evolution history of the system from constant-radius initiation to equilibrium propagation. Prior to the onset of interfacial peeling, as the internal pressure increases, the central deflection of the blister continuously rises, and the system ascends along a vertical line at a constant horizontal coordinate ($a/a_c = 1$). Once the local release rate reaches the critical value ($G = G_c$), the simulated data points transition to and conform closely with the equilibrium propagation curve given by Eq. (13). Fig. 4(b) validates the combined effects of different interlayer and substrate slip parameters at a fixed fracture toughness ($G_c = 0.3\,\mathrm{N/m}$). Fig. 4(c) and (d) reveal the scaling effect of fracture toughness ($G_c = 0.1, 0.2, 0.3\,\mathrm{N/m}$) on the peeling trajectory under fixed interfacial shear-lag parameters ($\ell = \ell_* = 1.0\,\mathrm{nm}$ and $5.0\,\mathrm{nm}$), indicating that a larger G_c necessitates a larger aspect ratio for the system at the same debonding radius.

Synthesizing the above comparison results reveals the following mechanical pattern: regarding the mechanism regulating the geometric evolution of peeling, the influence of interlayer slip is significantly stronger than that of substrate slip. From a physical perspective, the strength of the interlayer shear dictates the relative proportion of the internal membrane stretching strain energy and bending strain energy within the multilayer system, thereby fundamentally dominating the geometric characteristics and power-law relations of the response curves between the two limits of pure stretching (membrane) and bending (plate). By contrast, substrate slip does not alter the membrane-like or plate-like attributes of the system; rather, it affects the peeling response solely by changing the effective constraint stiffness of the substrate. A smoother substrate leads to a weaker effective boundary constraint on the system, resulting in greater flexural deformation at the same blister radius, which is intuitively manifested graphically as an overall vertical elevation of the curve.

3.2. Load–displacement response and Q–B approximation

Based on the full-field higher-order perturbation solutions (provided in Section S2 of the Supplementary material), the load–displacement response of the multilayer blister during the equilibrium propagation stage — namely, the evolutionary relationship between the central deflection h and the internal blister pressure p — can be further derived:

$$\frac{pa^4}{h^3 t_\dagger} = B(\kappa, \kappa_*, \nu)E + \frac{\kappa^2}{\kappa^2 + 16}\frac{64 D_0}{t_\dagger^3}\left(\frac{t_\dagger}{h}\right)^2, \tag{20}$$

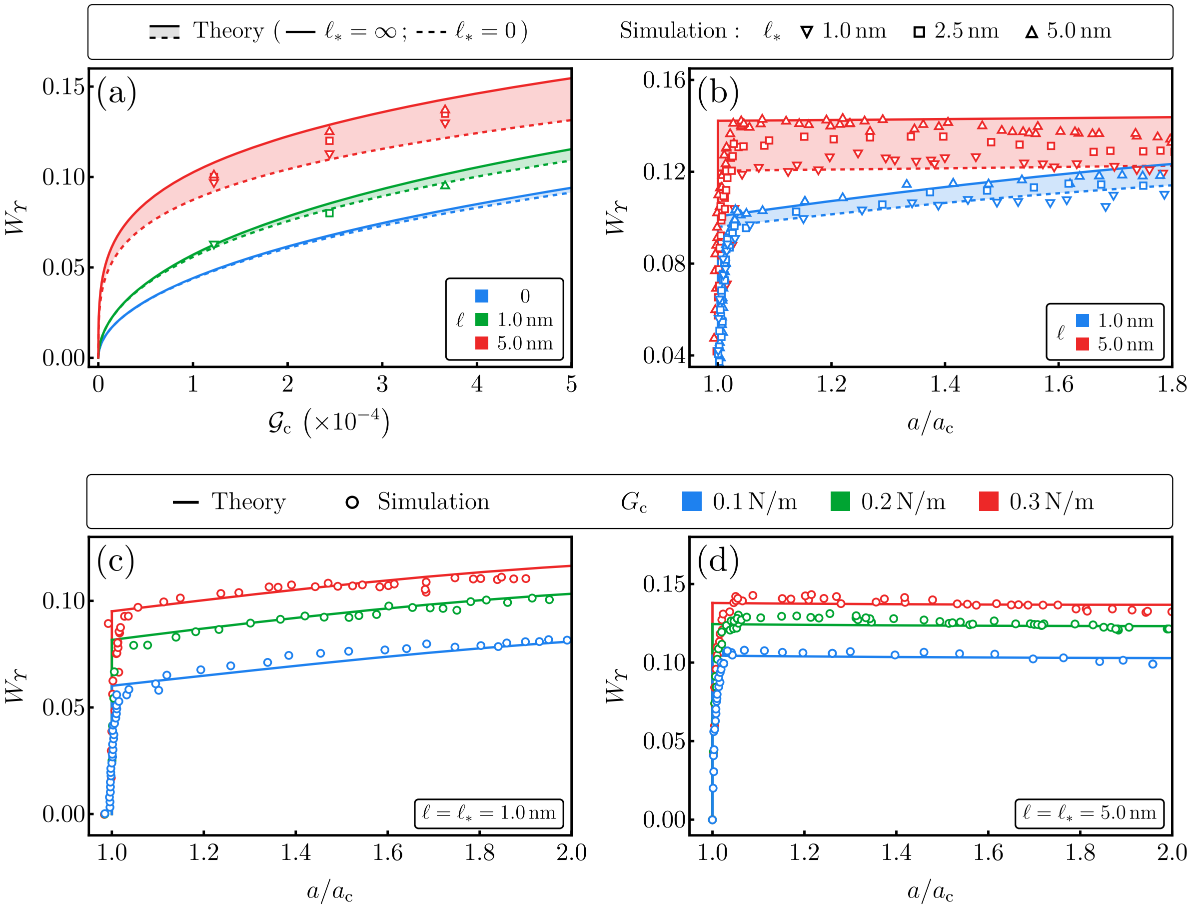

Fig. 4. Comparison between theoretical predictions and MD simulations of the multilayer blister peeling aspect ratio. Subfigure (a) illustrates the variation of the critical aspect ratio with the dimensionless substrate interfacial fracture toughness $\mathcal{G}_c$. The blue, green, and red envelope bands correspond to $\ell = 0, 1.0, 5.0$ nm, respectively, with their upper bound solid lines and lower bound dashed lines representing absolutely smooth ($\ell_* = \infty$) and perfectly bonded ($\ell_* = 0$) substrates. The hollow scattered points denote the MD validations for finite-friction substrates (hollow down-triangles, squares, and up-triangles sequentially correspond to $\ell_* = 1.0, 2.5, 5.0$ nm). Subfigures (b)–(d) track the complete evolution of the aspect ratio with the normalized radius a/a_c: the vertical line segments correspond to the constant-radius pressurization process prior to initiation, and the curved segments correspond to the quasi-static peeling governed by $G = G_c$. Subfigure (b) compares the combined effects of different interfacial slip parameters, while (c) and (d) demonstrate the scaling effect of the fracture toughness G_c on the peeling aspect ratio under specific slip conditions, respectively.

where the dimensionless stretching load coefficient function (briefly referred to as the stretching load coefficient) $B(\kappa, \kappa_*, \nu)$ governing the large-deflection response takes the analytical form:

$$B(\kappa,\kappa_*,\nu) = -\frac{1}{\kappa_*}\frac{K_1(\kappa_*)}{K_2(\kappa_*)}\frac{8(\kappa^4+32\kappa^2+384)(5\kappa^4+144\kappa^2+1152)}{27(\kappa^2+16)^4}\frac{1+\nu}{1-\nu} + \frac{2}{135(\kappa^2+16)^4(1-\nu)}\left[\begin{array}{c}\kappa^8(173-73\nu)+8\kappa^6(1229-469\nu)\\ +3840\kappa^4(59-19\nu)+92160\kappa^2(27-7\nu)\\ +2211840(5-\nu)\end{array}\right]. \tag{21}$$

Given that the exact analytical expressions for both the stretching release rate coefficient Q and the stretching load coefficient B are highly cumbersome, with the mathematical structure of Q being substantially more complex than that of B, a single-variable dimension-reduced approximation for the function ratio Q/B is introduced here to circumvent the inconvenience of handling high-dimensional complex analytical formulas in subsequent analysis and computation:

$$\frac{Q(\kappa,\kappa_*,\nu)}{B(\kappa,\kappa_*,\nu)} \approx 0.40265 + \frac{27695}{(\kappa^2+35.084)^{3.3156}} = \Theta(\kappa). \tag{22}$$

Extensive random sampling and numerical assessments across the full physical parameter space confirm that this one-dimensional approximation bounds the maximum relative error within ±2% (with the vast majority of samples converging within ±0.5%). The detailed global error analysis and error contour maps are provided in Section S4 of the Supplementary material. While strictly preserving analytical precision, this compact dimension-reduced mathematical form provides a direct and comprehensive mathematical tool for the subsequent analyses of the peeling response scaling law, the snap-through instability mechanism, and the construction of system phase diagrams across the full parameter space.

To explore the load–displacement relationship throughout the entire pressurized blistering and peeling stages, a full-history analysis is conducted in conjunction with Eq. (20). During the initial pressurization stage prior to initiation, the central deflection h has not yet reached the critical peeling aspect ratio state $W_Y(a_c)$. At this point, the load–displacement relationship is determined directly according to Eq. (20) by adopting a constant radius $a = a_c$. As h increases to the critical value $h_c = W_Y(a_c)a_c$, interfacial peeling initiates, and the subsequent load–displacement relationship must treat the continuously evolving current radius a as a parametric variable, described by the following system of equations ($a \in (a_c, +\infty)$):

$$\begin{cases} \dfrac{pa^4}{h^3 t_\dagger} = B(\kappa,\kappa_*,\nu)E + \dfrac{\kappa^2}{\kappa^2+16}\dfrac{64D_0}{t_\dagger^3}\left(\dfrac{t_\dagger}{h}\right)^2 \\ \dfrac{h}{a} = W_Y = \left(\dfrac{\sqrt{1+\beta^2}-1}{\beta}\right)^{\frac{1}{2}}\left[\dfrac{\mathcal{G}_c}{Q(\kappa,\kappa_*,\nu)}\right]^{\frac{1}{4}} \end{cases} \tag{23}$$

Eliminating a from the above two equations yields the explicit relations for p and G_c:

$$\begin{cases} p = \dfrac{\kappa^2}{\kappa^2+16}64D_0\dfrac{W_Y^4}{h^3} + B(\kappa,\kappa_*,\nu)E_{2D}^\dagger\dfrac{W_Y^4}{h} \\ G_c = \dfrac{32\kappa^4}{(\kappa^2+16)^2}D_0\dfrac{W_Y^4}{h^2} + Q(\kappa,\kappa_*,\nu)E_{2D}^\dagger W_Y^4 \end{cases} \tag{24}$$

Dividing the two equations directly extracts the inverse scaling law of the pressure p evolving with the central deflection h during the quasi-static peeling stage:

$$p = \Lambda(\kappa,\kappa_*,\nu,\lambda)\frac{G_c}{h}, \tag{25}$$

where the analytical expression for the scaling coefficient Λ is:

$$\Lambda(\kappa,\kappa_*,\nu,\lambda) = \frac{\frac{64\kappa^2}{\kappa^2+16} + B(\kappa,\kappa_*,\nu)\lambda}{\frac{32\kappa^4}{(\kappa^2+16)^2} + Q(\kappa,\kappa_*,\nu)\lambda}. \tag{26}$$

The dimensionless parameter $\lambda = E_{2D}^\dagger h^2/D_0 \sim U_s/U_b^\infty$ is introduced in the above equation. Given that D_0 represents the equivalent upper limit of the bending stiffness for the multilayer system under perfect interlayer bonding ($\kappa \to \infty$), the dimensionless parameter λ characterizes, in a scaling sense, the relative magnitude of the in-plane stretching strain energy U_s to the theoretical maximum reference bending strain energy U_b^∞ under large-deflection nonlinear deformation.

Under the purely stretching moment-free membrane limit ($\kappa \to 0, \lambda \to \infty$), the inverse proportionality coefficient in Eq. (25) can be degenerated to $\Lambda \approx \Theta^{-1}(0) \approx 1.64$ using the approximation Eq. (22); whereas under the purely bending plate limit ($\kappa \to \infty, \lambda \to 0$), it degenerates to an exact constant $\Lambda = 2$. For general multilayer coupled cases involving finite interfacial friction, based on the physical intuition derived from the aforementioned two classical limits, it can be reasonably conjectured that the inverse scaling law $p \propto G_c/h$ remains widely valid. A rigorous analytical demonstration for this conjecture is provided below.

From the energy balance criterion for quasi-static peeling (Eq. (12)), it can be derived that:

$$\mathcal{G}_c = \left[\frac{32\kappa^4}{(\kappa^2+16)^2}\lambda + Q(\kappa,\kappa_*,\nu)\lambda^2\right]\frac{1}{\mathcal{K}^2}, \tag{27}$$

Denoting the denominator of the function Λ in Eq. (26) as Λ_{dnm}, Eq. (27) can be further condensed to $\lambda\Lambda_{dnm} = \mathcal{G}_c\mathcal{K}^2$. If there existed a singular point causing Λ to diverge during actual physical evolution, it would necessarily require the denominator $\Lambda_{dnm} \to 0$. However, the right-hand side of the equation, $\mathcal{G}_c\mathcal{K}^2$, is a deterministic non-zero positive number at the onset of blister initiation, which forces $\lambda \to \infty$. But once $\lambda \to \infty$, since the stretching release rate coefficient $Q > 0$, the denominator Λ_{dnm} inevitably diverges toward infinity, posing a direct mathematical contradiction with the prerequisite $\Lambda_{dnm} \to 0$. Therefore, the system energy constraint during the peeling process fundamentally precludes the physical possibility of $\Lambda_{dnm} = 0$, absolutely ensuring that Λ must be a bounded quantity.

To further quantitatively demonstrate that the proportionality coefficient satisfies $\Lambda = \mathcal{O}(1)$, a phase-space mapping analysis is introduced in this section. Leveraging the previously established high-precision approximation Eq. (22), the originally four-parameter-dependent Λ can be dimension-reduced and simplified into a bivariate function depending exclusively on κ and a new composite variable $Y := B\lambda$:

$$\Lambda(\kappa,\kappa_*,\nu,\lambda) \approx \frac{\frac{64\kappa^2}{\kappa^2+16} + Y}{\frac{32\kappa^4}{(\kappa^2+16)^2} + \Theta(\kappa)Y} := \Lambda(\kappa, Y). \tag{28}$$

This dimension-reduced mapping enables a visual inspection of the global distribution of the comprehensive coefficient Λ via a two-dimensional phase diagram. Fig. 5(a) plots the contour map of the reduced $\Lambda(\kappa, Y)$ values. The contour distribution in the figure intuitively verifies the preceding limit analysis: in the low-κ, high-Y regime representing the pure membrane limit (top-left of the phase diagram) and the high-κ, low-Y regime representing the pure plate limit (bottom-right), the values of Λ stably converge near $\Theta^{-1}(0) \approx 1.64$ and 2, respectively, in excellent agreement with the degenerated theories. However, a localized numerical divergent singularity peak exists at the bottom-center of the contour map. To prove that the actual macroscopic peeling history can automatically bypass this singular peak, thereby maintaining $\Lambda = \mathcal{O}(1)$, the system evolution trajectories constrained by the energy criterion must be superimposed onto the phase diagram.

To map the dimensionless energy constraint equation (Eq. (27)) into an equation containing solely the phase-space coordinates (κ, Y) via algebraic transformations, the hidden variable involving the current blister radius a must be eliminated, thereby yielding the trajectory equation uniquely determined by the system's intrinsic material and structural parameters:

$$\frac{32Y}{(\kappa^2+16)^2} + \Theta(\kappa)\left(\frac{Y}{\kappa^2}\right)^2 = B\left(\kappa, \frac{\sqrt{N+1}}{2\sqrt{3}}\frac{\ell}{\ell_*}\kappa, \nu\right)C_{\mathrm{mat}}, \tag{29}$$

where a comprehensive structural-material parameter $C_{\mathrm{mat}} = \mathcal{G}_{\mathrm{c}}\left[\frac{E_{2\mathrm{D}}^{\dagger}}{D_0}\frac{N(N+1)}{12}\ell^2\right]^2$ incorporating only system constants is defined.

To quantitatively visualize the physical picture, material parameters consistent with the subsequent MD simulations (detailed in Section S5 of the Supplementary material) are adopted, setting $\ell = \ell_*$ and the interfacial fracture toughness to $G_{\mathrm{c}} = 0.1\,\mathrm{N/m}$. The evolution trajectories under various values of C_{mat} are plotted in the phase diagram of Fig. 5(a). The arrows on the trajectories indicate the evolution direction as the blister radius a expands. The peeling energy criterion dictates that the debonding radius satisfies $a \geq a_{\mathrm{c}}$. The white dash-dotted line (critical envelope) in the figure is the lower-bound envelope constructed by extracting and smoothly connecting the initial state points corresponding to the critical initiation radius $a_{\mathrm{c}} = 5\,\mathrm{nm}$ on each trajectory (Eq. (29)) under different comprehensive constants C_{mat}. This boundary divides the phase space into an upper physically accessible domain and a lower inaccessible domain that violates the energy criterion, thereby keeping the starting points of the evolution trajectories away from the divergent peak region. Within the accessible domain above the critical curve, the values of Λ remain within 10 (the pure white area in the legend color bar corresponds to $\Lambda = 10$). Considering that the magnitude of the intrinsic mechanical parameters adopted in this example is consistent with 2D material systems, and the critical initiation radii observed in actual multilayer 2D material blister experiments are typically on the order of hundreds of nanometers to micrometers — far exceeding the 5 nm selected in this example — the physical critical boundary corresponding to actual systems will be significantly higher than the position depicted in the figure, embedding the divergent peak region even deeper within the physically inaccessible domain. This proves that during the quasi-static debonding process of multilayer 2D materials, the peeling scaling coefficient rigorously satisfies $\Lambda = \mathcal{O}(1)$.

Fig. 6 presents a comparison between the theoretical predictions and MD simulation results of the load–displacement response for multilayer blisters. In the purely analytical plots (Figs. 6(a) and 6(b)), different colored bands denote distinct interlayer shear-lag characteristic lengths ℓ. The upper bound solid line and lower bound dashed line of a band of the same color correspond to the absolutely smooth ($\ell_* = \infty$) and perfectly bonded ($\ell_* = 0$) substrate limits, respectively, outlining the evolution boundaries for a given ℓ value.

Fig. 6(a) tracks the dimensionless load–displacement response history of the blister from constant-radius pressurization prior to initiation, across the critical point, and into quasi-static peeling. The results reflect the disparate impacts of the two interfacial slip mechanisms on the response: interlayer slip (ℓ) dominates the global stiffness and strength of the system, whereas substrate slip (ℓ_*) merely induces minor translations within the interlayer envelope bands. This phenomenon aligns with the preceding physical analysis: interlayer slip dictates the energy partitioning mechanism between stretching and bending within the system, while substrate slip only weakens the tangential constraint stiffness in the supported region, leading to larger flexural deformations under the same pressure (manifested graphically as a slight upward shift of the curve with increasing ℓ_*). As ℓ increases from 1 nm to 5 nm, the global bending capacity of the system degrades, and the nonlinear characteristics in the pre-initiation stage intensify. Upon entering the quasi-static peeling stage, all evolution curves exhibit the scaling law feature of $p \propto G_{\mathrm{c}}/h$.

To further analyze the mechanical features of the peeling stage, Fig. 6(b) extracts the evolution trajectory of the scaling coefficient $\Lambda = ph/G_{\mathrm{c}}$ with respect to the normalized debonding radius a/a_{c}. Observing the evolution bands under various ℓ, a non-monotonic evolution of Λ with ℓ can be identified: when the interlayer constraint degenerates from perfect bonding ($\ell = 0$, dark blue dash-dotted line, pure plate limit $\Lambda = 2$) to the absolutely smooth pure membrane limit ($\ell = \infty$, dark red dash-dotted line, $\Lambda = \Theta^{-1}(0) \approx 1.64$), the scaling coefficient does not decrease monotonically. In the finite friction regime (e.g., $\ell = 1\,\mathrm{nm}, 2\,\mathrm{nm}$), the scaling coefficient first rises to a peak and then gradually declines (e.g., $\ell = 5\,\mathrm{nm}$), ultimately converging to the pure membrane limit of 1.64. This non-monotonic evolution stems from the antagonistic coupling of the system's stretching and bending strain energies under finite interlayer shear, and its pattern aligns with the characteristics exhibited when moving along the critical envelope in the phase diagram of Fig. 5(a). Figs. 6(c) and 6(d) supplement the validation results comparing continuum theoretical predictions and MD simulation data for the full-range peeling history under different boundary combinations. By altering the interlayer shear-lag parameter ($\ell = 1, 3, 5\,\mathrm{nm}$, Fig. 6(c)) and the fracture toughness ($G_{\mathrm{c}} = 0.1, 0.2, 0.3\,\mathrm{N/m}$, Fig. 6(d)), the theoretical analytical solutions (solid lines) agree well with the MD simulation data (scattered points).

The aforementioned cross-validation confirms the universality of the load scaling law extracted in this study. Regarding the load response characteristics, the inverse scaling law $p \propto G_{\mathrm{c}}/h$ established through the dimension-reduced approximation in this study is consistent with relevant experimental and theoretical observations. For instance, based on contact resonance atomic force

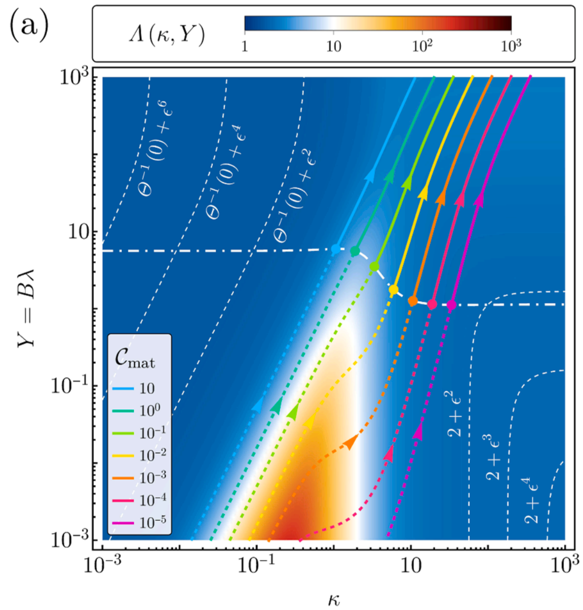

Fig. 5. Dimensionless phase diagrams and definition of physical evolution domains for the peeling response and instability analysis. Subfigure (a) illustrates the contour map of the scaling coefficient $\Lambda(\kappa, Y)$, reflecting the applicability of the inverse scaling law $p \propto G_c/h$ within the physically accessible regime. Subfigure (b) displays the contour map of the critical instability volume ratio $\chi_c(\kappa, Y)$, providing a quantitative criterion for constant-source peeling instability across the full parameter space. The thin white dashed lines in both contour maps are contour lines; for concise labeling, a minor parameter $\epsilon = 10^{-1}$ is introduced in their numerical markings. Superimposed on both figures are the physical evolution trajectories governed by the comprehensive constant C_{mat} (colored solid lines with arrows indicating the evolution direction of blister debonding propagation). The white dash-dotted line (critical curve) connects the initial state points corresponding to $a_c = 5\,\mathrm{nm}$ on each trajectory, representing the physical lower bound of the system; the phase space below this boundary is an inaccessible domain constrained by the energy release criterion.

microscopy (CR-AFM) mechanical mapping of 2D nanoblisters, Ma et al. (2024) observed an evolution law wherein the equilibrium internal pressure of the blister is inversely proportional to its geometric characteristic dimension. Extended Hencky analytical solutions targeting the single-layer film peeling problem (Ma et al., 2018; Yin et al., 2024) also yielded a similar load attenuation trend. However, existing analytical studies are predominantly based on the single-layer pure membrane assumption that neglects bending stiffness. By utilizing the Q–B dimension-reduced approximation, the present analysis demonstrates that this inverse scaling law remains applicable to multilayer systems coupled with large-deflection geometric nonlinearity and multiple interfacial shear-lag effects. By distilling the macroscopic physical scaling from complex multivariate transcendental functions, this analytical treatment offers a practical theoretical reference for the interfacial mechanical characterization of multilayer 2D materials.

3.3. Constant-source snap-through instability

As indicated by the load–displacement response in the previous section, the multilayer blister follows an inverse-proportional softening law $p \propto 1/h$ during the quasi-static peeling stage. This implies that if the system is driven by a constant pressure at the critical peeling point, once the initiation condition is met, the blister will undergo unstable propagation, and the system will lose its load-bearing capacity. However, in 2D material blister experiments, the load is typically applied by controlling the total number of gas molecules within a closed cavity, referred to as "constant pre-pressure" or "constant-source loading." Under this condition, due to the finite volume of the closed cavity, the expansion of the blister volume will lead to the attenuation of the current pressure p within the cavity. This section explores the geometric criterion and evolution behavior of the system's instability under the constant-source loading path.

Let V_0 be the dead volume of the gas cavity and V_b be the bulging volume of the blister. According to the ideal gas law, the constant initial source pressure p_0 and the current actual pressure p are related as follows:

$$p_0 = p\left(1 + \frac{V_b}{V_0}\right). \tag{30}$$

From this equation, the aforementioned constant pressure loading is physically strictly equivalent to the infinite cavity volume limit ($V_0 \to \infty$), where the actual pressure no longer attenuates with the increasing blister volume ($p = p_0$). For a general case with a finite cavity volume ($V_0 < \infty$), the axisymmetric blister volume can be obtained by integrating the deflection profile function as $V_b = 2\pi \int_0^a wr\,\mathrm{d}r = \frac{\pi a^2 h}{3}\frac{\kappa^2+24}{\kappa^2+16}$. Substituting this and the previously derived pressure formula (Eq. (25)) into Eq. (30), the control

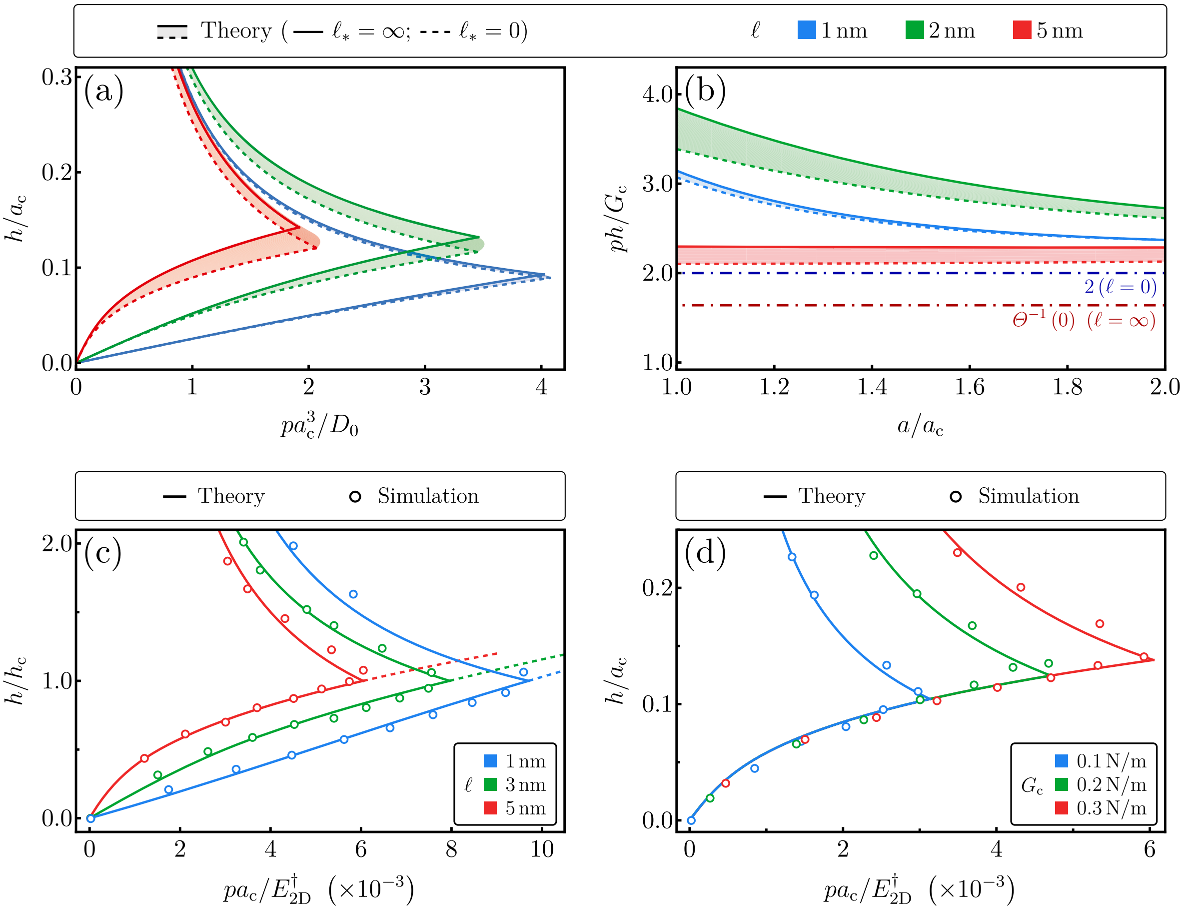

Fig. 6. Load–displacement response and MD simulation validation of multilayer blisters during the complete loading and quasi-static peeling stages. Subfigure (a) illustrates the evolution history of dimensionless pressure versus central deflection. The different colored bands represent distinct interlayer decoupling characteristic lengths ℓ, with the upper bound solid lines and lower bound dashed lines delineating the mechanical boundaries under absolutely smooth ($\ell_* = \infty$) and perfectly bonded ($\ell_* = 0$) substrate conditions, respectively. Subfigure (b) presents the evolution of the scaling coefficient $\Lambda = ph/G_c$ with the normalized radius a/a_c during peeling. The dark blue and dark red dash-dotted lines represent the theoretical benchmarks of the pure plate limit ($\ell = 0$) and the pure membrane limit ($\ell = \infty$), respectively, reflecting the non-monotonic feature of Λ first increasing and then decreasing with a growing ℓ. Subfigures (c) and (d) show the agreement between continuum theoretical solutions (solid lines) and MD simulation data (hollow circular scattered points) under controlled interlayer slip length ℓ (fixed G_c, ℓ_*) and varied interfacial fracture toughness G_c (fixed ℓ, ℓ_*), respectively.

variable p_0 can be expressed as a function of the central deflection h and the peeling aspect ratio W_Y:

$$p_0 = G_c \Lambda(\kappa, Y)\left(\frac{1}{h} + \frac{\pi h^2}{3W_Y^2 V_0}\frac{\kappa^2+24}{\kappa^2+16}\right). \tag{31}$$

Since both the shear factor κ and the peeling aspect ratio W_Y depend on the debonding radius a, and according to the quasi-static propagation equation (Eq. (13)), a and h are nonlinearly coupled. Therefore, it is impossible to directly eliminate a from Eq. (31) to extract a global explicit function $p_0(h)$. To this end, the instability characteristics under the two limits of a "moment-free membrane" and a "pure bending plate" are first analyzed, followed by a discussion of the general case involving finite shear interactions.

Under the moment-free membrane limit ($\kappa \to 0, \lambda \to \infty$), as established in Eq. (15), the peeling aspect ratio simplifies to $W_Y = [\mathcal{G}_c/Q(0, \kappa_*, \nu)]^{1/4}$. If the substrate is further assumed to be absolutely smooth ($\kappa_* = 0$) or perfectly bonded ($\kappa_* \to \infty$), W_Y degenerates to a constant. Consequently, the source pressure evolution equation (Eq. (31)) simplifies to:

$$p_0 = \frac{G_c}{\Theta(0)}\left(\frac{1}{h} + \frac{\pi h^2}{2W_Y^2 V_0}\right). \tag{32}$$

Setting $\partial p_0/\partial h = 0$ yields the critical characteristic deflection corresponding to the extremum point, $h_s^{(m)} = (W_Y^2 V_0/\pi)^{1/3}$. When $h < h_s^{(m)}$ (equivalent to $\pi a^2\ h < V_0$), the source pressure strictly decreases; when $h > h_s^{(m)}$, it strictly increases. Therefore, if the critical geometry at initiation satisfies $\pi a_c^2 h_c \geq V_0$ (i.e., $h_c \geq h_s^{(m)}$), the central deflection during the peeling stage steadily increases with the source pressure. Conversely, if $\pi a_c^2 h_c < V_0$, once the source pressure reaches the initiation threshold, the central deflection of the system will jump to the next stable equilibrium point along a constant-source-pressure path, triggering snap-through instability.

Similarly, under the pure plate limit ($\kappa \to \infty, \lambda \to 0$), the energy criterion requires $W_Y = [G_c/(32D_0)]^{1/4}\sqrt{h}$. Substituting this alongside the peeling scaling coefficient $\Lambda = 2$ for simplification yields:

$$p_0 = 2G_c\left[\frac{1}{h} + \frac{\pi h}{3V_0}\left(\frac{32D_0}{G_c}\right)^{1/2}\right]. \tag{33}$$

Setting $\partial p_0/\partial h = 0$ derives the characteristic critical deflection under the plate limit as $h_s^{(p)} = \left(3W_Y^2 V_0/\pi\right)^{1/3}$. Combining this with the initiation condition $G_c/(32D_0) = h_c^2/a_c^4$, the geometric criterion for instability is obtained: if $\pi a_c^2 h_c \geq 3V_0$, the peeling evolves stably; if $\pi a_c^2 h_c < 3V_0$, a snap-through instability occurs.

For general cases involving finite shear, the global evolution of the initial source pressure p_0 with respect to the blister volume V_b must be examined to establish an instability criterion. Following interfacial initiation, the system evolves along a physical trajectory constrained by the release rate $G = G_c$. The critical instability point corresponds to the extremum condition $\mathrm{d}p_0/\mathrm{d}V_b|_{V_0^{\text{crit}}, V_b^{\text{crit}}} = 0$. Differentiating $p_0(V_b) = p(V_b)(1 + V_b/V_0)$ and setting it to zero solves for the critical dead volume V_0^{crit} that triggers instability:

$$V_0^{\text{crit}} = -V_b^{\text{crit}}\left[1 + \frac{p(V_b^{\text{crit}})}{V_b^{\text{crit}}\, p'(V_b^{\text{crit}})}\right]. \tag{34}$$

Defining the local softening rate (power-law exponent) m along the peeling evolution path as:

$$m = \frac{V_b}{p}\frac{\mathrm{d}p}{\mathrm{d}V_b}, \tag{35}$$

the critical dead volume can be expressed as $V_0^{\text{crit}} = -V_b^{\text{crit}}\frac{m+1}{m}$. Define a dimensionless critical instability volume ratio $\chi_c = \pi a_c^2 h_c / V_0^{\text{crit}}$, and express the critical blister volume as $V_b^{\text{crit}} = \alpha(\kappa)\pi a_c^2 h_c$, where the morphological factor is $\alpha(\kappa) = (\kappa^2 + 24)/[3(\kappa^2 + 16)]$. Substituting these into Eq. (35) yields:

$$\chi_c(\kappa, B\lambda) = \frac{-m}{\alpha(\kappa)(m+1)}. \tag{36}$$

This equation signifies that the critical volume ratio is exclusively determined by the local softening rate m and the morphological factor α. Under the membrane limit, the peeling aspect ratio is constant ($a \propto h$), leading to the volume $V_b \propto h^3$. Combined with $p \propto h^{-1}$, the pressure satisfies $p \propto V_b^{-1/3}$, yielding $m = -1/3$. Substituting this and the membrane-limit morphological factor $\alpha(0) = 1/2$ into Eq. (36) yields $\chi_c = 1$. Under the pure plate limit, $a \propto h^{1/2}$, yielding the volume $V_b \propto h^2$. The pressure then satisfies $p \propto V_b^{-1/2}$, meaning $m = -1/2$. Substituting this and the plate-limit factor $\alpha(\infty) = 1/3$ yields $\chi_c = 3$. The results under these two limits perfectly match the preceding explicit extremum analyses.

To compute the softening rate m for general parameters within the phase space, a constant constraint function along the evolution trajectory can be extracted:

$$\mathcal{F}(\kappa, Y) = \frac{1}{B(\kappa)}\left[\frac{32Y}{(\kappa^2+16)^2} + \Theta(\kappa)\left(\frac{Y}{\kappa^2}\right)^2\right] \equiv \text{const}, \tag{37}$$

where $B(\kappa) = B\left(\kappa, \frac{\sqrt{N+1}}{2\sqrt{3}}\frac{\ell}{\ell_*}\kappa, \nu\right)$. The slope of the trajectory in the (κ, Y) space is $Y' = -(\partial\mathcal{F}/\partial\kappa)/(\partial\mathcal{F}/\partial Y)$.

To calculate the local softening rate $m = \frac{V_b}{p}\frac{\mathrm{d}p}{\mathrm{d}V_b}$ along the evolution trajectory, the material and structural constants within the pressure and blister volume that are independent of the state variables (κ, Y) must be separated. The dimensionless characteristic pressure $\hat{p}$ and characteristic volume $\hat{V}_b$, which depend solely on the phase coordinates, are extracted as:

$$\hat{p} = \frac{\Lambda(\kappa, Y)\sqrt{B(\kappa)}}{\sqrt{Y}}, \quad \hat{V}_b = \alpha(\kappa)\kappa^2\sqrt{\frac{Y}{B(\kappa)}}. \tag{38}$$

After expressing the complete physical quantities as the products of dimensional structural constant factors and the aforementioned characteristic functions, substituting them into the definition of the softening rate naturally cancels out the constant prefixes during the division of the relative rates of change. Consequently, the calculation of m can be strictly transformed into a logarithmic differential form of these dimensionless characteristic quantities:

$$m = \frac{\mathrm{d}(\ln\hat{p})}{\mathrm{d}(\ln\hat{V}_b)} = \frac{\frac{\partial\ln\hat{p}}{\partial\kappa} + \frac{\partial\ln\hat{p}}{\partial Y}Y'}{\frac{\partial\ln\hat{V}_b}{\partial\kappa} + \frac{\partial\ln\hat{V}_b}{\partial Y}Y'}. \tag{39}$$

Substituting m into Eq. (36) yields the distribution of the critical volume ratio, as shown in Fig. 5(b). The χ_c value plateaus in the top-left region (membrane limit) and bottom-right region (pure plate limit) of the phase diagram converge to the asymptotic values of 1 and 3, respectively. Thus, this phase diagram provides a unified geometric criterion for constant-source peeling instability across the full parameter space: if the initiation geometry and the dead volume of the cavity satisfy $\frac{\pi a_c^2 h_c}{V_0} < \chi_c$, a snap-through instability occurs at the instant of peeling; otherwise, it manifests as stable propagation.

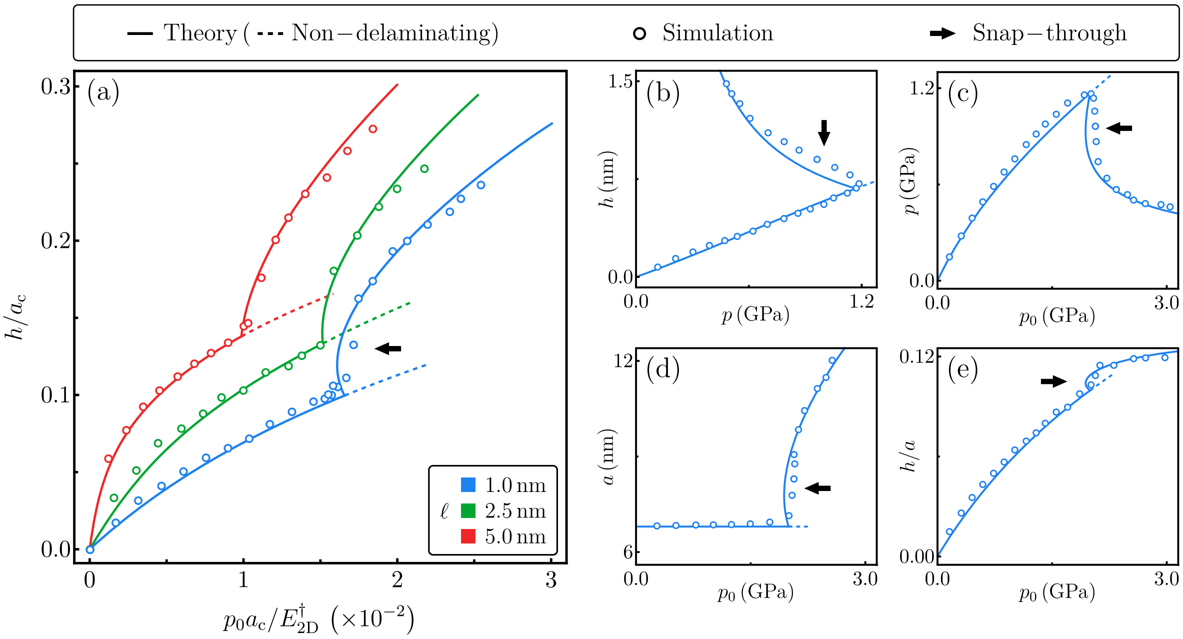

Fig. 7. Theoretical curves and MD simulation validation of the multilayer blister snap-through instability behavior under constant-source loading. Subfigure (a) illustrates the variation of the dimensionless central deflection with the initial source pressure p_0 under different interlayer characteristic lengths ℓ. The short dashed lines represent the hypothetical non-delaminating branches, whereas the solid lines represent the complete physical evolution paths. Subfigures (b)-(e) display the relationships between central deflection and current pressure ($h - p$), current pressure and initial source pressure ($p - p_0$), debonding radius and source pressure ($a - p_0$), and peeling aspect ratio and source pressure ($h/a - p_0$) at $\ell = 1.0\,\text{nm}$, respectively. The discrete hollow circles in the figures denote MD simulation data, while the bold black arrows indicate the snap-through paths of the system under constant-source conditions.

Fig. 7 compares the theoretical predictions and MD simulation results for the multilayer blister evolution response and snap-through instability under constant-source loading. In Fig. 7(a), as the interlayer shear-lag length ℓ increases, the system behavior transitions: at $\ell = 1.0\,\text{nm}$, the theoretical peeling branch emerges with a negative slope at the initiation point, indicating snap-through instability. As ℓ increases from $1.0\,\text{nm}$ to $5.0\,\text{nm}$, this negative-slope feature gradually vanishes, and the peeling branch becomes monotonically increasing, corresponding to stable peeling. Fig. 7(b) to (e) trace the evolution trajectories of various physical quantities when snap-through instability occurs at $\ell = 1.0\,\text{nm}$. The MD simulation data reveal that after the system is loaded to the initiation point, it undergoes a discontinuous jump, landing directly on the next stable equilibrium branch. These results demonstrate that the instability criterion defined in this study accurately captures the snap-through instability characteristics constrained by a finite cavity volume.

In fact, for blister peeling under constant-source loading conditions, previous mechanical analyses based on the single-layer pure membrane assumption (Ma et al., 2018; Yin et al., 2024) primarily focused on the responses during the stable evolution stage. However, based on the physical consensus of interfacial fracture in confined systems, a snap-through instability is inevitably triggered when the system's cavity volume ratio crosses a specific critical threshold. A key theoretical insight elucidated by this study is how the macroscopic bending resistance, generated by interlayer shear mediating in-plane stretching gradients, quantitatively regulates the triggering boundary of this snap-through instability. Because traditional single-layer pure membrane models exclude intrinsic bending stiffness, applying them directly to predict extremum instability in multilayer systems will inevitably result in a theoretical misjudgment of the critical volume ratio. Relying on the analytically extracted local softening exponent, the full-parameter phase diagram established in this study systematically quantifies how multiple interfacial slips reshape the instability threshold. These findings not only clarify the physical applicability boundaries of existing pure membrane theories but also provide a quantitative mechanical evaluation criterion for failure avoidance in confined micro/nano systems under constant-source loading.

4. Conclusions

Focusing on the blister peeling of multilayer 2D structures coupled with multiple interfacial slips, this study establishes a comprehensive analytical model for moving-boundary debonding evolution within the framework of configurational variational theory. The primary theoretical advancements and physical findings are summarized as follows:

First, at the theoretical level of configurational mechanics, a structural-level Eshelby configurational stress tensor coupling in-plane stretching, out-of-plane bending, and transverse shear effects is constructed for multilayer 2D structures governed by dual interfacial slips under large-deflection deformation. Furthermore, utilizing the asymptotic perturbation fields, the explicit analytical expression for the interfacial energy release rate of this multiple-slip system is derived. This derivation effectively extends the configurational mechanics approach to the large-deflection multilayer blister model encompassing out-of-plane geometric nonlinearity, providing a self-consistent configurational driving force description for the geometric migration of the peeling front.

Second, regarding the fracture criterion and geometric evolution, a quasi-static equilibrium peeling criterion for multilayer blisters is established based on the aforementioned energetic description. The study reveals that the aspect ratio evolution during the quasi-static peeling stage is exclusively governed by the intrinsic structural and material parameters of the system. During this process, the interlayer shear interaction generates macroscopic bending resistance by mediating the in-plane stretching gradients, thereby fundamentally dictating the peeling aspect ratio of the blister. By contrast, the substrate slip merely fine-tunes the peeling behavior by weakening the boundary constraint stiffness.

Finally, concerning the load response and snap-through instability behavior, an explicit simplification of the multivariate transcendental function ratio is achieved by introducing a dimension-reduced approximation. On this basis, the inverse scaling law $p \propto G_c/h$ during the quasi-static peeling stage is established. Furthermore, under the physical premise of constant-source loading (i.e., fixed gas mass), a critical volume ratio jointly determined by the local softening exponent and the blister morphological factor is defined. By plotting the phase diagram across the full parameter space, the geometric criterion for snap-through instability triggered by multiple shear-lag effects is quantitatively revealed.

Ultimately, this study establishes the analytical link between the underlying mechanical fields and the global configurational driving force in the slip-coupled multilayer blister system. The analysis quantifies the dependence of the quasi-static peeling evolution and instability characteristics on multiple shear-lag effects. The developed framework thereby serves as a theoretical reference for the interfacial mechanical characterization and structural design of multilayer 2D materials and general layered film systems.

CRediT authorship contribution statement

Xiangtian Shen: Writing – review & editing, Writing – original draft, Visualization, Validation, Software, Methodology, Investigation, Formal analysis, Data curation, Conceptualization; **Zhaohe Dai:** Writing – review & editing, Supervision, Methodology; **Yueguang Wei:** Writing – review & editing, Supervision, Resources, Project administration, Methodology, Funding acquisition, Conceptualization.

Declaration of competing interest

The authors declare that they have no known competing financial interests or personal relationships that could have appeared to influence the work reported in this paper.

Acknowledgments

This work was supported by the Grants of NSFC (Nos. 12432003 and 12032001), and the National Science and Technology Major Project of China (Grant No. J2022-V-0003-0029). X. Shen is grateful to Prof. Yong Ma (Beihang University) and Prof. Yin Zhang (Peking University) for their insightful discussions and valuable suggestions.

Data availability

Data will be made available on request.

Supplementary material

Supplementary material associated with this article can be found in the online version at 10.1016/j.jmps.2026.106842.

References

Ai, R., Cui, X., Li, Y., Zhuo, X., 2025. Local strain engineering of two-dimensional transition metal dichalcogenides towards quantum emitters. Nano-Micro Lett. 17, 104. https://doi.org/10.1007/s40820-024-01611-1

Brotons-Alcázar, I., Terreblanche, J.S., Giménez-Santamarina, S., Gutiérrez-Finol, G.M., Ryder, K.S., Forment-Aliaga, A., Coronado, E., 2024. Atomic force microscopy beyond topography: chemical sensing of 2D material surfaces through adhesion measurements. ACS Appl. Mater. Interfaces 16, 19711–19719. https://doi.org/10.1021/acsami.3c19254

Cui, X., Liu, L., Dong, W., Zhou, Y., Zhang, Z., 2023. Mechanics of 2D material bubbles. Nano Res. 16 (12), 13434–13449. https://doi.org/10.1007/s12274-023-6060-9

Dai, Z., Hou, Y., Sanchez, D.A., Wang, G., Brennan, C.J., Zhang, Z., Liu, L., Lu, N., 2018. Interface-governed deformation of nanobubbles and nanotents formed by two-dimensional materials. Phys. Rev. Lett. 121 (26), 266101. https://doi.org/10.1103/PhysRevLett.121.266101

Dai, Z., Rao, Y., Lu, N., 2022. Two-dimensional crystals on adhesive substrates subjected to uniform transverse pressure. Int. J. Solids Struct. 257, 111829. https://doi.org/10.1016/j.ijsolstr.2022.111829

Eshelby, J.D., 1951. The force on an elastic singularity. Philosophical Trans. Royal Soc. Lond., Ser. A 244, 87–112. https://doi.org/10.1098/rsta.1951.0016

Geng, Y., Yang, J., Yang, Y., 2026. 2D nanomaterials toward function-ready superlubricity in advanced microsystems. Adv. Mater. , e20679. https://doi.org/10.1002/adma.202520679

Guo, Y., Zhang, P., Liu, Y., Liu, Z., Liu, J., Liu, A., Wu, D., Pan, Z., Ding, H., Yu, S., Zhang, X., Wu, F., Hong, Y., Wang, Z., Ren, T.-L., Tian, H., 2026. A towards-foundry strategy for creating fully interconnected two-dimensional microprocessors. Nat. Electr. 9, 159–169. https://doi.org/10.1038/s41928-026-01573-9

Gurtin, M.E., 2000. Configurational Forces as Basic Concepts of Continuum Physics. Applied Mathematical Sciences, Springer New York, New York, NY. https://doi.org/10.1007/b97847

Hu, R., Song, J., Huang, W., Zhou, A.-n., Lin, J.-l., Cao, Y., Hu, S., 2025. Controlling interfacial adhesion during the transfer of large-area 2D materials: mechanisms, strategies, and research advances. New Carbon Mater. 40, 553–583. https://doi.org/10.1016/S1872-5805(25)60988-7

Huang, Z., He, Z., Zhu, Y., Wu, H., 2023. A general theory for the bending of multilayer van der Waals materials. J. Mech. Phys. Solids 171, 105144. https://doi.org/10.1016/j.jmps.2022.105144

Kim, D.H., Yoo, J., Suh, H.C., Won, Y.S., Kim, S.H., Yi, D.-J., Jeong, B.G., Lee, C., Lee, D., Kim, K.K., Lee, S.M., Koh, E.K., Jeong, M.S., 2025. Anomalous phonon softening with inherent strain in wrinkled monolayer WSe2. Adv. Mater. 37, 2419414. https://doi.org/10.1002/adma.202419414

Lee, H.Y., Sarkar, S., Reidy, K., Kumar, A., Klein, J., Watanabe, K., Taniguchi, T., LeBeau, J.M., Ross, F.M., Gradečak, S., 2022. Strong and localized luminescence from interface bubbles between stacked hBN multilayers. Nature Commun. 13, 5000. https://doi.org/10.1038/s41467-022-32708-z

Li, B., Tan, W., Shen, C., Long, Y., Gao, Z., Wang, J., Guo, W., Yin, J., 2024. Bending stiffness of ionically bonded mica multilayers told by its bubbles. J. Mech. Phys. Solids 190, 105723. https://doi.org/10.1016/j.jmps.2024.105723

Li, N., Wu, H., Sun, C., Zhao, J., 2025. Adhesion of 2D materials: measurement and modulation. Acta Mech. Solida Sinica 38, 252–274. https://doi.org/10.1007/s10338-024-00552-x

Liu, H., Chen, Y., Wang, W., Liu, L., Liu, Y., Zheng, Q., 2025. Homogenization of two-dimensional materials integrating monolayer bending and surface layer effects. J. Mech. Phys. Solids 194, 105911. https://doi.org/10.1016/j.jmps.2024.105911

Liu, Z., Long, J., Cao, H., 2026a. Interlayer slip engineering induces unexpected out-of-plane piezoelectricity in group-VA nanosheets. Small 22, e13710. https://doi.org/10.1002/smll.202513710

Liu, Z., Zhu, L., Yuan, S., Zhang, Y., Zhang, P., Cai, Z., Liu, L., Yang, R., 2026b. Functional 2D MoS2 NEMS resonator array with independent electronic tunability based on mass transfer printing. Microsyst. Nanoeng. 12, 21. https://doi.org/10.1038/s41378-025-01132-w

Long, Y., Jiang, Z., Gao, Z., Li, B., Li, X., Liu, X., Yin, J., Guo, W., 2023. Bubbles as a platform for investigating work function tunability of 2D materials under biaxial strains. Extreme Mech. Lett. 60, 101978. https://doi.org/10.1016/j.eml.2023.101978

Ma, C., Yang, X., Chen, Y., Chu, J., 2024. Mechanical mapping of nanoblisters confined by two-dimensional materials reveals complex ridge patterns. Langmuir 40, 8409–8417. https://doi.org/10.1021/acs.langmuir.3c03879

Ma, Y., Wang, G., Chen, Y., Long, D., Guan, Y., Liu, L., Zhang, Z., 2018. Extended Hencky solution for the blister test of nanomembrane. Extreme Mech. Lett. 22, 69–78. https://doi.org/10.1016/j.eml.2018.05.006

Qin, H., Yan, Y., Liu, H., Liu, J., Zhang, Y.-W., Liu, Y., 2020. Modified Timoshenko beam model for bending behaviors of layered materials and structures. Extreme Mech. Lett. 39, 100799. https://doi.org/10.1016/j.eml.2020.100799

Rao, Y., Kim, E., Dai, Z., He, J., Li, Y., Lu, N., 2023. Size-dependent shape characteristics of 2D crystal blisters. J. Mech. Phys. Solids 175, 105286. https://doi.org/10.1016/j.jmps.2023.105286

Rice, J.R., 1968. A path independent integral and the approximate analysis of strain concentration by notches and cracks. J. Appl. Mech. 35, 379–386. https://doi.org/10.1115/1.3601206

Sanchez, D.A., Dai, Z., Lu, N., 2021. 2D material bubbles: fabrication, characterization, and applications. Trends Chem. 3 (3), 204–217. https://doi.org/10.1016/j.trechm.2020.12.011

Sanchez, D.A., Dai, Z., Wang, P., Cantu-Chavez, A., Brennan, C.J., Huang, R., Lu, N., 2018. Mechanics of spontaneously formed nanoblisters trapped by transferred 2D crystals. Proc. Natl. Acad. Sci. 115 (31), 7884–7889. https://doi.org/10.1073/pnas.1801551115

Schätz, J., Nayi, N., Weber, J., Metzke, C., Lukas, S., Walter, J., Schaffus, T., Streb, F., Reato, E., Piacentini, A., Grundmann, A., Kalisch, H., Heuken, M., Vescan, A., Pindl, S., Lemme, M.C., 2024. Button shear testing for adhesion measurements of 2D materials. Nature Commun. 15, 2430. https://doi.org/10.1038/s41467-024-46136-8

Shen, X., Wei, Y., 2026. Bulge mechanics of pre-tensioned multilayer 2D structures with interlayer and substrate slip. Int. J. Solids Struct. 338, 114102. https://doi.org/10.1016/j.ijsolstr.2026.114102

Thomas, R.M., Mishra, A., Shahin, S., Khan, M.S., Khan, Z.H., 2026. Advanced Nanomaterials in Electrical and Electronics Miniaturization. Springer Nature Singapore, Singapore. pp. 157–219. https://doi.org/10.1007/978-981-95-3600-9_6

Vidhi, F., Yadav, P., 2026. Advanced Materials for Self-Powered Gas Sensors. Springer Nature Switzerland, Cham. pp. 67–84. https://doi.org/10.1007/978-3-032-09625-8_4

Wang, D., Yu, D., Chen, H., Zhao, C., Chen, X., Lu, M., 2025. The influence of different nanoscale channel lengths in low-temperature-grown lateral MoS_2 memristors. ACS Appl. Mater. Interfaces 17, 69719–69728. https://doi.org/10.1021/acsami.5c21337

Wang, G., Dai, Z., Xiao, J., Feng, S., Weng, C., Liu, L., Xu, Z., Huang, R., Zhang, Z., 2019. Bending of multilayer van der Waals materials. Phys. Rev. Lett. 123 (11), 116101. https://doi.org/10.1103/PhysRevLett.123.116101

Wang, W., Ma, X., Dai, Z., Zhang, S., Hou, Y., Wang, G., Li, Q., Zhang, Z., Wei, Y., Liu, L., 2022. Mechanical behavior of blisters spontaneously formed by multilayer 2D materials. Adv. Mater. Interfaces 9 (12), 2101939. https://doi.org/10.1002/admi.202101939

Yao, Z., Deng, J., Li, L., 2024. Piezoelectric performance regulation from 2D materials to devices. Matter 7, 855–888. https://doi.org/10.1016/j.matt.2023.12.031

Yildirim, T., Liu, B., Baines, D., Lu, Y., 2025. Nanoscale engineering of non-uniform biaxially strained domes. npj 2D Mater. Appl. 9, 111. https://doi.org/10.1038/s41699-025-00628-3

Yin, Y., Dang, R., Wu, D., Li, M., Li, Y., Gao, H., 2024. Mechanics of microblister tests in 2D materials accounting for frictional slippage. Carbon 229, 119495. https://doi.org/10.1016/j.carbon.2024.119495

Yu, C., Zeng, W., Wang, B., Cui, X., Gao, Z., Yin, J., Liu, L., Wei, X., Wei, Y., Dai, Z., 2025. Stiffer is stickier: adhesion in elastic nanofilms. Nano Lett. 25, 1876–1882. https://doi.org/10.1021/acs.nanolett.4c05309

Yu, X., Peng, Z., Xu, L., Shi, W., Li, Z., Meng, X., He, X., Wang, Z., Duan, S., Tong, L., Huang, X., Miao, X., Hu, W., Ye, L., 2024. Manipulating 2D materials through strain engineering. Small 20, 2402561. https://doi.org/10.1002/smll.202402561

Yue, K., Gao, W., Huang, R., Liechti, K.M., 2012. Analytical methods for the mechanics of graphene bubbles. J. Appl. Phys. 112 (8), 083512. https://doi.org/10.1063/1.4759146

Zeng, W., Dai, Z., Wei, Y., 2026. Adhesion of elastic membranes. Part I: a generalized tabor parameter. Proc. Roy. Soc. A Math. Phys. Eng. Sci. 482, 20250932. https://doi.org/10.1098/rspa.2025.0932

Zhu, G., Zhang, T., Huang, H., Xie, X., Shi, X., Jie, J., Wang, T., Du, W., 2026. In operando reconfigurable exciton–plasmon coupling via strain engineering. Laser Photonics Rev. 20, e02782. https://doi.org/10.1002/lpor.202502782